Marine Geology 449 (2022) 106836

Contents lists available at ScienceDirect

Marine Geology

journal homepage: www.elsevier.com/locate/margo

Understanding the retreat of the Jurassic Cantabrian coast (N. Spain): Comprehensive monitoring and 4D evolution model of the Tazones Lighthouse landslide

M.J. Domínguez-Cuesta [a,*], P. González-Pumariega [b], P. Valenzuela [c], C. López-Fernández [a], L. Rodríguez-Rodríguez [a], D. Ballesteros [d], M. Mora [e], M. Meléndez [f], F. Herrera [a], M.A. Marigil [g], L. Pando [a], J. Cuervas-Mons [a], M. Jiménez-Sánchez [a]

[a] University of Oviedo, Departamento de Geología, Oviedo, Spain
[b] University of Oviedo, Departamento de Explotación y Prospección de Minas, Mieres, Spain
[c] University of Cantabria, Departmento de Ciencias de la Tierra y Física de la Materia Condensada, Santander, Spain
[d] University of Granada, Departamento de Geodinámica, Spain
[e] Territorial Delegation in Castilla y León, State Meteorological Agency of Spain, Valladolid 47014, Spain
[f] Instituto Geológico y Minero de España, Oviedo, Spain
[g] Instituto Geográfico Nacional, Oviedo, Spain

ARTICLE INFO

Keywords:
Coastal cliff retreat
Jurassic Cantabrian Coast
Landslide monitoring
Maritime storms
Rainfall influence

ABSTRACT

Forecasting coastal dynamics and sea cliff retreat under different sea level rise scenarios requires a good understanding of the conditioning factors and their relative contribution to cliff stability. The so-called Jurassic Cantabrian Coast extends along 76 km of the coastline of the Asturias region (N Spain) and is well-known worldwide due to its paleontological heritage, in particular the presence of dinosaur remains and footprints. The abundance of stratigraphic, paleontological and tectonic studies contrasts with the scarcity of studies focused on the stability of this rocky coastline where cliffs predominate, sometimes exceeding 120 m in height. In fact, evidence of current and recent instability processes can be observed along the entire coastline. In this regard, continuous monitoring is crucial to understand ongoing instabilities in rocky coastlines, as in these settings some instabilities might initiate as slow movements that induce subtle topographic changes whose detection from either satellite or aerial imagery is problematic due to the spatial and temporal resolutions. This contribution presents a 4D evolution model of a key site, the Tazones Lighthouse landslide, located on the Cantabrian Coast of Asturias (N Spain), which affects subvertical rocky cliffs sculpted in the Jurassic bedrock made of alternating sandstone and marl. A high resolution multiapproach methodology was developed in order to understand its structure and kinematic characteristics, including: i) interpretation of aerial photographs and unmanned aerial photogrammetric surveys (UAV); ii) 22 monthly monitoring campaigns by total station; iii) 5 manual boreholes; iv) geomechanical characterization of the cliff bedrock; v) geomorphological evidence mapping; vi) analysis of landscape deformations obtained from UAV; and vii) precipitation, soil moisture and significant wave height (H_s) data analysis. The results show that the slope evolves by means of a complex-type mass movement, which combines translational and sliding mechanisms, and occupies tens of thousands of square meters. DTM and fieldwork analysis indicate that mass movement is mainly controlled by bedrock discontinuities (S0, 360/15-17; J1, 262/85; J2 166/75). The most important accelerations of slope movement correlate very well with rainfall, soil moisture and waves. Thus, the largest displacements occurring in January and October–November 2019, coincide with 2 periods of storms (maximum 24-h rainfall of 64.5 mm and 82.1 mm and maximum H_s of 6.54 and 9.09, respectively) and soil moisture values above 90%. Half of the markers moved more than 1 m and one of them exceeded 15 m. The 4D model obtained after the interpretation of the Tazones Lighthouse slope whole

* Corresponding author.
E-mail addresses: dominguezmaria@uniovi.es (M.J. Domínguez-Cuesta), pelayogs@uniovi.es (P. González-Pumariega), pablo.valenzuela@unican.es (P. Valenzuela), lopezcarlos@uniovi.es (C. López-Fernández), rodriguezrlaura@uniovi.es (L. Rodríguez-Rodríguez), dballesteros@ugr.es (D. Ballesteros), mmoray@aemet.es (M. Mora), m.melendez@igme.es (M. Meléndez), ferhermol93@gmail.es (F. Herrera), miguelangel.marigil@correo.gob.es (M.A. Marigil), pandoluis@uniovi.es (L. Pando), jcuervas@geol.uniovi.es (J. Cuervas-Mons), mjimenez@uniovi.es (M. Jiménez-Sánchez).

https://doi.org/10.1016/j.margeo.2022.106836
Received 2 November 2021; Received in revised form 13 May 2022; Accepted 17 May 2022
Available online 26 May 2022

dataset, allows an understanding of how the surrounding cliffs have evolved in the past, fundamental to predicting their future behaviour.

1. Introduction

Coasts are very sensitive to environmental and climatic changes and respond very quickly to them. The EUROSION project of the European Parliament (EUROSION, 2004) concluded that 25% of European coasts are subject to a retreat dynamic due to the action of different processes and natural factors like the action of waves and maritime storms on rocky coasts (Trenhaile, 2014). At least a quarter of the world's population lives in areas near steep coasts (Small and Nicholls, 2003) affected by coastal retreat and the progress of this retreat depends on the nature and structure of the rock as well as the type and intensity of the weathering and erosion processes (Trenhaile, 1987; Sunamura, 1992; Del Río and Gracia, 2009; Piacentini et al., 2021). A more in-depth analysis shows that the retreat of coastal cliffs is due to the interaction

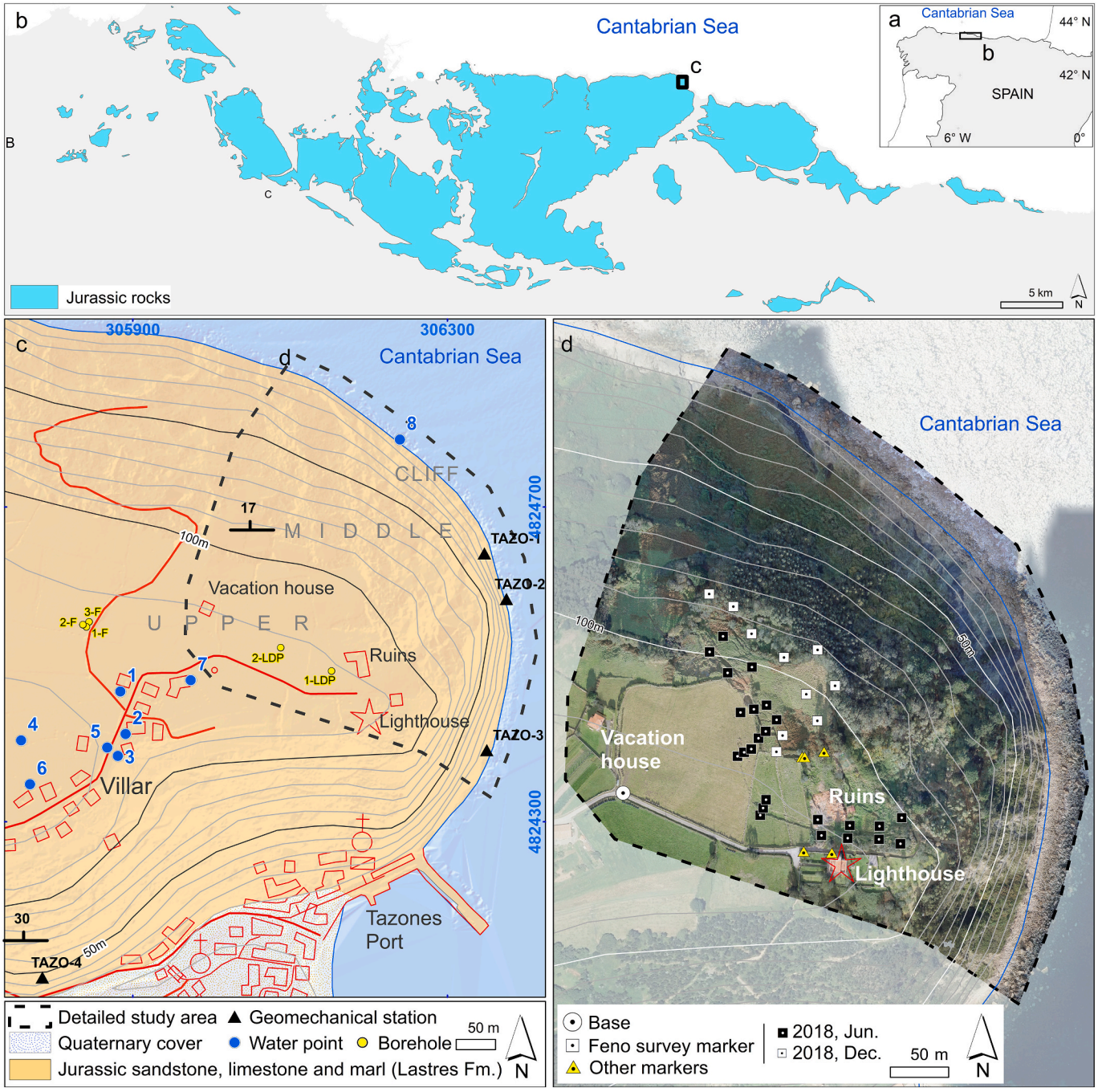

Fig. 1. **a.** Location of the Jurassic bedrock on the Spanish Cantabrian Coast. **b.** Distribution of the Jurassic bedrock (Merino Tomé et al., 2013). **c.** Lithological map (Pignatelli et al., 1972), parts of the slope and location of water points and geomechanical stations in the study area. Terrain model: LIDAR-PNOA 2012 CC-BY 4.0 scne.es. **d.** Position of the monitored topographic markers. Background image: OrtoPNOA 2017 CC-BY 4.0 scne.es. UTM coordinates ETRS89, Zone 30.

of several factors and processes (Blanco-Chao et al., 2007; Trenhaile, 2011) that act at different spatial and temporal scales (Troiani et al., 2020). On a large scale, phenomena such as tectonic activity and climate change, with direct impacts on mean sea level, storm frequency, precipitation or wind regime and wave patterns can exert control over the general evolution of the coastline (Kennedy et al., 2014; Jongejan et al., 2016; Trenhaile, 2018). The current rate of coastal retreat does not appear to match the average rate measured since the Holocene. For instance, some estimated cliff retreat rates since the mid-Holocene on the Normandy coastline (from 0.051 ± 0.008 to 0.090 ± 0.014 m y^{-1}) are between 33% and 57% lower than those currently measured (Duguet et al., 2021). Some authors argue that the retreat is not continuous, but occurs episodically, associated with discrete receding events from the top of the cliff hundreds of years apart (Mushkin et al., 2019). Two types of processes act on these materials (Castedo et al., 2013): (i) marine processes, which mainly affect the base of the cliffs, and (ii) subaerial processes, which act on the exposed area; their relative contribution varies over time and space. The joint action of abrasion and wave quarrying generated by sea waves, together with the erosive and weathering processes controlled by the climate, give rise to slope instability phenomena of different magnitude and typology, which constitute the most important agent of coastal retreat (e.g., Naylor and Stephenson, 2010; Gómez-Pazo et al., 2021). In this regard, geomorphological studies and periodic monitoring of coastline are essential to understand the variables that regulate cliff retreat and to predict its future evolution in response to climate change and related sea level rise (Van Maanen et al., 2016; Isaev et al., 2019).

The Cantabrian Coast, located in the North of the Iberian Peninsula, is an 800 km-long rocky coast with *E*-W trending linearity. Almost 25% of its extent corresponds to rocky cliffs included in the Asturias region, where slope instabilities are frequent (Valenzuela et al., 2017; Domínguez-Cuesta et al., 2018a, 2018b). Numerous studies have focused on the sandy reaches of the Cantabrian Coast, comprising their evolution and sand loss issues (Flor and Flor-Blanco, 2005; De Sanjosé Blasco et al., 2018). By contrast, few works have addressed the retreat of the rocky cliffs (Domínguez-Cuesta et al., 2020a, 2020b). There is consensus that the Cantabrian Coast has been retreating over the last two decades, particularly the coast reaches involving Jurassic bedrock (the so-called Cantabrian Jurassic Coast in which the present work focuses), though the rates remain largely unquantified in detail and the mechanisms involved in regulating the style and pace of retreat remain poorly known. A better understanding of these aspects is crucial for defining the suitability of future actions to be implemented in response to coastal retreat: Defence, Accommodation or Retreat (DAR, Williams et al., 2018). Among the actions mentioned, defensive investments costing millions of euros have already been carried out on the Cantabrian Jurassic Coast (BOE, 2014; MITECO-Ministerio para la Transición Ecológica y el Reto Demográfico, 2021), often disregarding the mechanisms and factors that modulate cliff retreat rate, which are all-important and must be understood in order to avoid short-term measures with unforeseen results. Furthermore, and of no less importance, the interventions carried out must be environmentally friendly, as well as durable and useful (Morales et al., 2021).

The Cantabrian Jurassic Coast extends along 76 km of the Asturias region coastline (northern Spain). It has been intensely studied from a stratigraphic (Badenas et al., 2012), structural (Uzkeda et al., 2016) and palaeontological points of view (Avanzini et al., 2010; Piñuela et al., 2009), since Jurassic rocks tend to outcrop along the coast (Fig. 1). The abundance of geological studies mentioned contrasts with the scarcity of studies focused on the stability of this rocky coastline, where cliffs of several dozen metres predominate, sometimes exceeding 120 m. This is an important deficiency, considering that this part of the Cantabrian coastline is world famous for the presence of dinosaur footprints. In this regard, evidence of active and old instability processes is observed along the entire Cantabrian Jurassic Coast, the presence of scars, fresh escarpments devoid of vegetation or angular blocks at the cliff's foot being frequent. Occasionally, instability evidence has been recognized several hundred metres inland. This is the case in the vicinity of the Tazones Lighthouse, where a restaurant building located more than 200 m from the coastline was irreversibly damaged due to the progression of cracks associated to cliff retreat (Domínguez-Cuesta et al., 2020b).

A research team from the University of Oviedo has been analysing the evolution of the Tazones Lighthouse slope since June 2018. This area constitutes a case study of great interest since it allows the study of an active geomorphological process and the analysis of how the cliff behaves in real time. The continuous, monitoring of the surroundings of the Tazones Lighthouse constitutes a unique opportunity to understand the evolution of the Cantabrian Jurassic cliffs, and so predict their spatio-temporal evolution. The aims of this work are to: i) characterize the typology of the instability that affects the Tazones Lighthouse slope; ii) quantify spatially and temporally the displacement experienced between June 2018–May 2020; iii) establish the conditioning factors of its origin; and iv) establish the relationships between landslide displacement acceleration and rainfall, soil moisture, and wave height. This will make it possible to understand how the Jurassic rocks of the surroundings behave and establish the basis for an evolutionary model of the Jurassic Cantabrian coast, necessary for predicting future changes.

2. Regional setting

The study area includes 161,103 m^2 of the surroundings of the Tazones Lighthouse, located on the Cantabrian Coast, west of Tazones (Fig. 1), a small fishing village of approximately 200 inhabitants.

The climate is temperate Cfb, according to the Köppen-Geiger classification (Peel et al., 2007), with mild temperatures (annual mean of 13°C) and rainfall distributed throughout the year (1000 mm $year^{-1}$) without a dry season (García Couto, 2011). The vegetation cover is almost continuous, mainly composed of meadows, scrub and some eucalyptus plantations. Predominant winds and coastal drift in this area come from the West.

The Tazones Lighthouse (43°32′54″N, 5°23′57″W) is located 170 m inland and 110 m a.s.l., on a marine terrace (locally termed "*rasa*") (Domínguez-Cuesta et al., 2015). The bedrock is an alternation of sandstone (1–10 m), marl (5–15 m) and lutite (1–10 cm) layers of the Upper Jurassic Lastres Formation (Valenzuela et al., 1986; García-Ramos and Gutiérrez Claverol, 1995; García-Ramos and Aramburu, 2010) dipping 15–17°N. The sandstone layers present both quartz and carbonate cements that rapidly dissolve due to weathering, losing density and resistance (García-Ramos, 2013) and acquiring characteristic yellowish or ochre tones. The remarkable alterability of this rock, whose open porosity can exceed 25%, has been proven by accelerated ageing tests in the laboratory (Ruiz de Argandoña et al., 2005). According to Uzkeda et al. (2016), the Jurassic rocks of the region are affected by small-scale normal, reverse, thrust, and strike slip faults and open folds, preferentially located in the hanging wall of steep dipping faults. The normal faults are the predominant structures, with four preferred orientations: N*E*-SW, NW-SE, E-W and NNW-SSE. These fault systems can show variable dips, from 35°–45° to almost vertical. There are some references to the existence of jet mining along the Jurassic coast since the Middle Age (Bahamonde et al., 1986; Monte Carreño, 2004; López, 2012). Traditionally, local subsidence phenomena have been interpreted in this area as mining collapses (Crespo et al., 2008) but no evidence of mining has been found during this research in the surroundings of the Tazones Lighthouse. The Quaternary coverage present in the zone mainly corresponds to colluvium deposits thinner than 2 m.

A sector of 70,000 m^2, located between 0 and 110 m a.s.l. shows evidence of active mass movements of different types and sizes. The upper zone (Fig. 1c) has an approximately flat slope (15% of the surface tilting less than 10°). The slope increases towards the middle zone and the cliff area, where the inclinations are mainly between 10 and 50°, reaching values between 50 and 82°. The vegetation is grassy on the flat

Fig. 2. a. View of the Tazones Lighthouse surroundings at the time of the restaurant eviction on February 20th 2018, after the critical enlargement of the cracks. **b.** Detailed view of the cracks in the restaurant building at the date of eviction. The presence of cement in the wall shows the attempt to repair old cracks that had developed before. **c. d.** Two views showing the evolution of surface cracks in the Tazones Lighthouse area on April 26th 2019 and January 17th 2020, respectively.

zone, and arboreal (eucalyptus plantations) in the middle zone, being non-existent on the cliff.

The cliff is active and instability processes occur every year in the vicinity of Tazones, both close to the sea and further inland. Sometimes gravity processes involve large volumes of rock, with deep cracks appearing at the surface. These events and signs have been detected by local people and researchers (Valenzuela et al., 2017; Domínguez-Cuesta et al., 2019), but until recently they had not been described in detail. Since 2018, a multidisciplinary research team has carried out monthly monitoring of 38 control points around the cracks that affected the area near the Tazones Lighthouse (Fig. 1) (Domínguez-Cuesta et al., 2020b). Some of these cracks are recognizable in aerial photographs taken since 1984 (López-Toyos et al., 2021), but have been pervasive since 2018, with accelerated movement and damage to the structural integrity of a restaurant and the abandonment of some agricultural and livestock/grazing land (Domínguez-Cuesta et al., 2019, 2020b). For now, none of the other buildings in the neighbouring town of Villar are affected. Within the study area, there are only three constructions: a vacation house, a lighthouse and the ruins of the mentioned restaurant (Fig. 2).

3. Materials and methods

The materials and methods used in this work are detailed below. All the information has been managed by Geographical Information System, GIS (ArcGIS v10.3) in order to store, prepare and analyse all datasets.

3.1. Annual photogrammetric surveys by unmanned aerial vehicle (UAV)

Two photogrammetric surveys were completed by drone on November 17th 2018 and November 29th 2019, respectively, using a CÁRABO S3 (ICOM3D) drone fitted with a 24-megapixel camera (Sony α5100) and a 20 mm fixed lens. Flight planning was carried out using UAV-GeoFlip software and a total of 10 ground control points (GCPs) were installed beforehand. To achieve the correct exposure, the shutter speed was fixed (1/800 s), the aperture was varied slightly (f/5.6–6.3), and ISO was kept between 200 and 800. This system provided 167 images in 2018, and 162 in 2019. The photogrammetric processing was carried out with Agisoft Metashape software (v.1.5.2). Textured 3D point clouds with an average density of 25 points/m^2, Digital Surface Models (DSM) derived from 3D point clouds and high resolution orthophotos with a 2.5 cm of Ground Sampling Distance-GSD were obtained for each year. Regarding photogrammetric reconstruction accuracy, error estimation was performed by means of checkpoints (12 in 2018, 7 in 2019) using GNSS positioning through Topcon GR-3 receivers. The RMSE (root-mean-square error) values reached 1.44 cm (X), 1.60 cm (Y) and 3.43 cm (Z) in 2018; and 2.86 cm (X), 2.76 cm (Y) and 1.53 cm (Z) in 2019.

3.2. Photointerpretation and geomorphological mapping

To contextualize the study area, geomorphological mapping of a

Table 1
Dates of the 22 monitoring campaigns carried out and days elapsed between them.

Campaign number	Year	Month	Day	Days between campaigns
C1	2018	06	12	1st installation
C2	2018	07	11	29
C3	2018	07	27	16
C4	2018	10	9	75
C5	2018	11	19	40
C6	2018	12	18	28 (2nd installation)
C7	2019	01	17	31
C8	2019	02	15	29 (3rd installation)
C9	2019	03	22	35
C10	2019	04	26	35
C11	2019	05	24	28
C12	2019	06	24	31
C13	2019	07	24	30
C14	2019	09	20	58
C15	2019	10	18	28
C16	2019	11	18	31
C17	2019	12	12	24
C18	2020	01	17	36
C19	2020	02	14	28
C20	2020	03	13	28
C21	2020	04	17	35
C22	2020	05	18	31

coastline section of approximately 4.5 km, including the area of interest, was carried out at 1:15,000 scale. The geomorphological map was created by: i) field work and ii) photointerpretation based on aerial photographs (flights of 2011 and 2017 of the Spanish PNOA program, 2004–2019 CC-BY 4.0 scne.es) and images obtained in 2018 and 2019 by UAV. In addition, LIDAR derived DEM (LIDAR-PNOA 2018 CC-BY 4.0 scne.es) and Google Earth images (years 2001, 2003, 2011, 2014, 2015 and 2016) have been analysed. Following Knight et al. (2011) and references cited therein, processes and landforms have been classified from a genetic point of view, including coastal landforms (marine terraces, cliffs, and active cliff front), mixed landforms (blocks destabilized by gravity processes and remobilized by the sea), fluvial landforms (main courses), gravity landforms (landslide masses and open cracks) and polygenic landforms (defined here according to Kamp and Owen, 2022). Moreover, a detailed geomorphological map of the Tazones Lighthouse slope has been completed at 1:1500 scale. Evidence of active processes and associated landforms was identified and shown in detail in the 3D model developed from the UAV flight for the study area. Also, the use of a boat provided a general view of the cliff from the sea, allowing the location and description of some instability features that were inaccessible or unobservable in the 3D model due to their small scale or their location in shadow zones.

3.3. Geomechanical characterization of the cliff bedrock

The geomechanical description of the rock mass was performed at 4 study points located at the foot of the cliff (Fig. 1c). The joint families (faults, joints and bedding) and their representative parameters (roughness, opening, spacing, and water content) were studied. Moreover, given the inaccessibility of a large part of the slope, structural data from 8 points on the cliff's surface were obtained from the drone point cloud through the Compass plugin (Thiele et al., 2017) of the Cloud Compare software (v.2.10.2). This tool makes it possible to measure the position of structural planes contained in a point cloud. To determine the potential formation of wedges, rockslides or the triggering of instabilities, a geometric and kinematic analysis was conducted using Dips software (v. 7.018).

3.4. Topographical monitoring

Surface displacements were topographically measured by means of 34 feno-type markers and 4 additional control points (nails located in constructive elements), covering an area of 12,000 m^2 (Fig. 1d). A feno-type marker is an anchored survey marker specifically designed to guarantee its permanence on the ground over time. The location of markers was selected after a field reconnaissance and according to the distribution of the ground cracks. On June 12th 2018, 24 topographic markers were installed and, later, another 12 control points were added after the appearance of new cracks: 10 on December 18th 2018 and another 2 on February 15 th 2019. All markers were located at altitudes between 95 and 110 m a.s.l. From June 2018 to May 2020, a total number of 22 topographic monitoring campaigns were carried out with a variable periodicity of 16 to 75 days (Table 1), depending on weather conditions.

In order to facilitate the interpretation of the topographic measurements, an arbitrary coordinate system was adopted, so that the X-axis coincides with the direction in which the greatest displacements occur. The instrument used for observing the ground displacement was a Leica TC-407 total station (precision of distance measurement: 2 mm ± 2 ppm; precision of angular measurement: 7″). Given the observation methodology adopted, displacements under 2 cm were not considered significant.

Due to the rapid progression of the landslide, 2 control points were lost between January and February 2019 (FA1) and between November and December 2019 (ARB). For this reason, some markers might appear without data in some campaigns because they were either lost or damaged. For instance, control points CA8 and FA9 were damaged by a bulldozer. Also, there are gaps in the movement logs because some markers were installed during a second installation campaign.

3.5. Precipitation, soil moisture content and wave data

The precipitation data from 4 rain gauges (located 10–19 km from the landslide) of the Spanish Meteorological Agency – Agencia Estatal de Meteorología (AEMET) were extracted for the period January 2018–May 2020. Furthermore, in the context of this research, a new AEMET manual rain gauge was installed and managed by volunteers in a village 2.3 km away from the study area. It provided discontinuous data between November 2018 and January 2020 that were compared with those of the aforementioned permanent stations. It was found that the rain gauge located at a distance of 10 km (named 'Luces-Aspo', 43°03′10″ N, 5°17′33″ W) had a complete series of monthly-accumulated precipitation values with a good correspondence with those recorded at the new manual station. Therefore, the precipitation data registered in that rain gauge have been employed in this work. The cumulative precipitation between consecutive measurement campaigns was calculated and plotted in temporal arrays, to analyse the correlation between movement of the markers and cumulative precipitation.

Soil moisture content has been estimated by the analysis of the Available Water Capacity (AWC). This hydrological index, which has been previously proved to be suitable for the study of landslide-triggering processes (Valenzuela et al., 2018), has been calculated as a percentage of maximum pore water storing capacity of the soil volume limited by the depth of the vegetation roots. The analysed daily data have been extracted for the same period from Daily Water Balance Models developed by the Spanish AEMET agency (Botey and Moreno, 2012). Input data comprises: i) daily precipitation and insolation values from weather stations; ii) atmospheric pressure, temperature, relative humidity and wind speed data from HIRLAM numerical weather prediction model; iii) soil type and texture, according to the Natural Resources Conservation Service-United States Department of Agriculture (NRCS-USDA) Soil Taxonomy (NRCS-USDA-Natural Resources Conservation Service-United States Department of Agriculture, Soil Survey Staff, 2003); (iv) depth of the vegetation roots, following the land use database Corine Land Cover (IGN-Instituto Geográfico Nacional, 2006); and (v) slope values, obtained from a Digital Slope Model derived from LIDAR. Output data are continuous models in raster format (25 km^2 cell

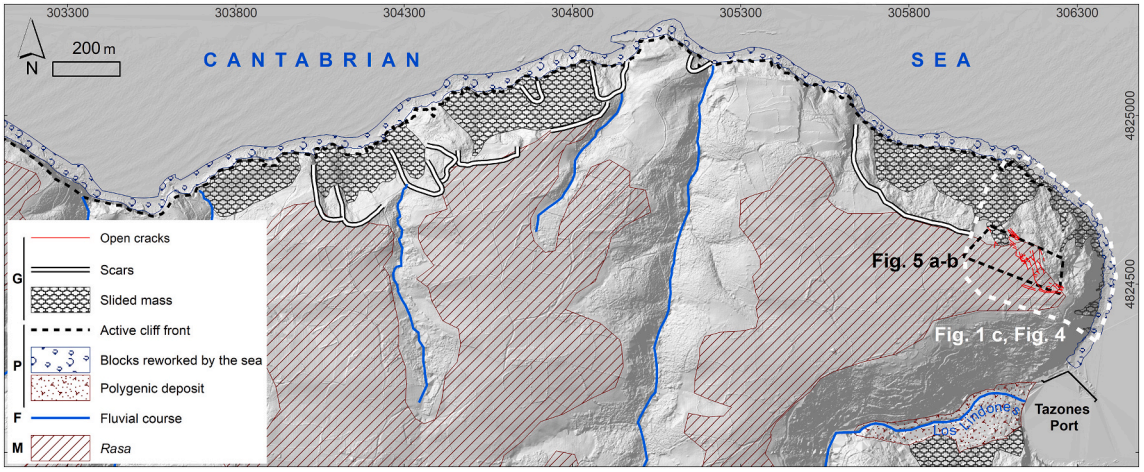

Fig. 3. Geomorphological map of the Jurassic coastal sector where the studied mass movement is located (origin of the landforms: G, gravity; P, polygenic; F, fluvial; M, marine). Open cracks and active cliff front are nowadays the most active geomorphological features.

size) obtained by kriging interpolation.

Significant wave height (H_s) data have been extracted from the Spanish State Ports (Puertos del Estado) SIMAR dataset (www.puertos.es), which contains time series of wave parameters from numerical modelling. Specifically, data have been obtained from SIMAR point 3,098,038 (5.42° W, 43.58°N), which is the closest to the study area. In this work, the hourly variation of the H_s parameter for the last 60 years has been used. Subsequently, for each day of the two year monitoring period, the maximum value of this parameter was extracted and plotted.

3.6. Execution of manual boreholes and water points recognition

Five boreholes were drilled with a manual Eijelkamp sampler to characterize the properties of the surficial formations present in the area. All of them were located on the *rasa* surface (Fig. 1c), two in areas where evidence of previous gravitational processes had been recognized: LPD-1 (UTM coordinates, ETRS89, Zone 30 T: 306153, 4,824,492; 113 m a.s.l.; 2.39 m deep) and LPD-2 (306,088, 4,824,521; 115 m a.s.l.; 1.40 m deep). The other three were in an area considered, a priori, stable: F-1 (305,841, 4,824,548; 117 m a.s.l.; 34 cm deep), F-2 (305,836, 4,824,550; 117 m a.s.l.; 61 cm deep), and F-3 (305,844, 4,824,554; 117 m a.s.l.; 1.01 m deep). The sedimentary sequence of the five cores was described and an infiltration test was carried out in boreholes F1 to F3 following the Porchet method.

The study area was also carefully searched to map evidence of springs and water table positioning. The depth at which the water table is found was measured in nearby wells for domestic use by means of a water probe on April 23th 2021.

4. Results

4.1. Geomorphological features

The new 1:15,000 scale cartography has enabled an in-depth description of the geomorphological features of the studied coastal segment and made it possible to contextualize the active instability evidence observed near the Tazones lighthouse.

The existence of a previously described ancient marine terrace (*rasa*) immediately apparent in the area (Fig. 3). The *rasa* has an average slope of 7°N. It is located between 90 and 150 m a.s.l. and delimited by cliffs

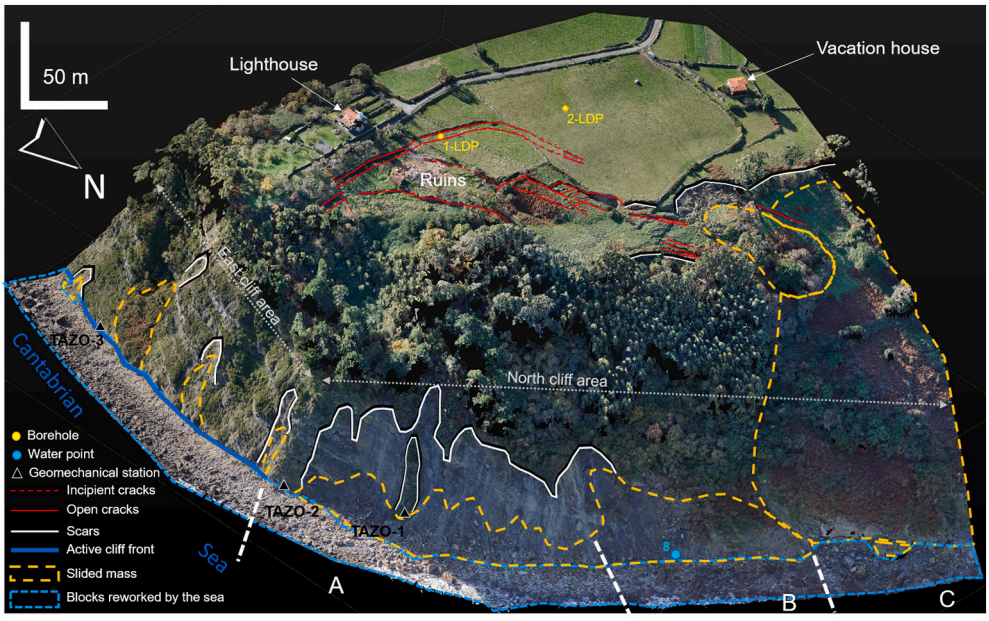

Fig. 4. 3D view of the main geomorphological features identified in the destabilized slope. Image taken by a drone flight in 2019.

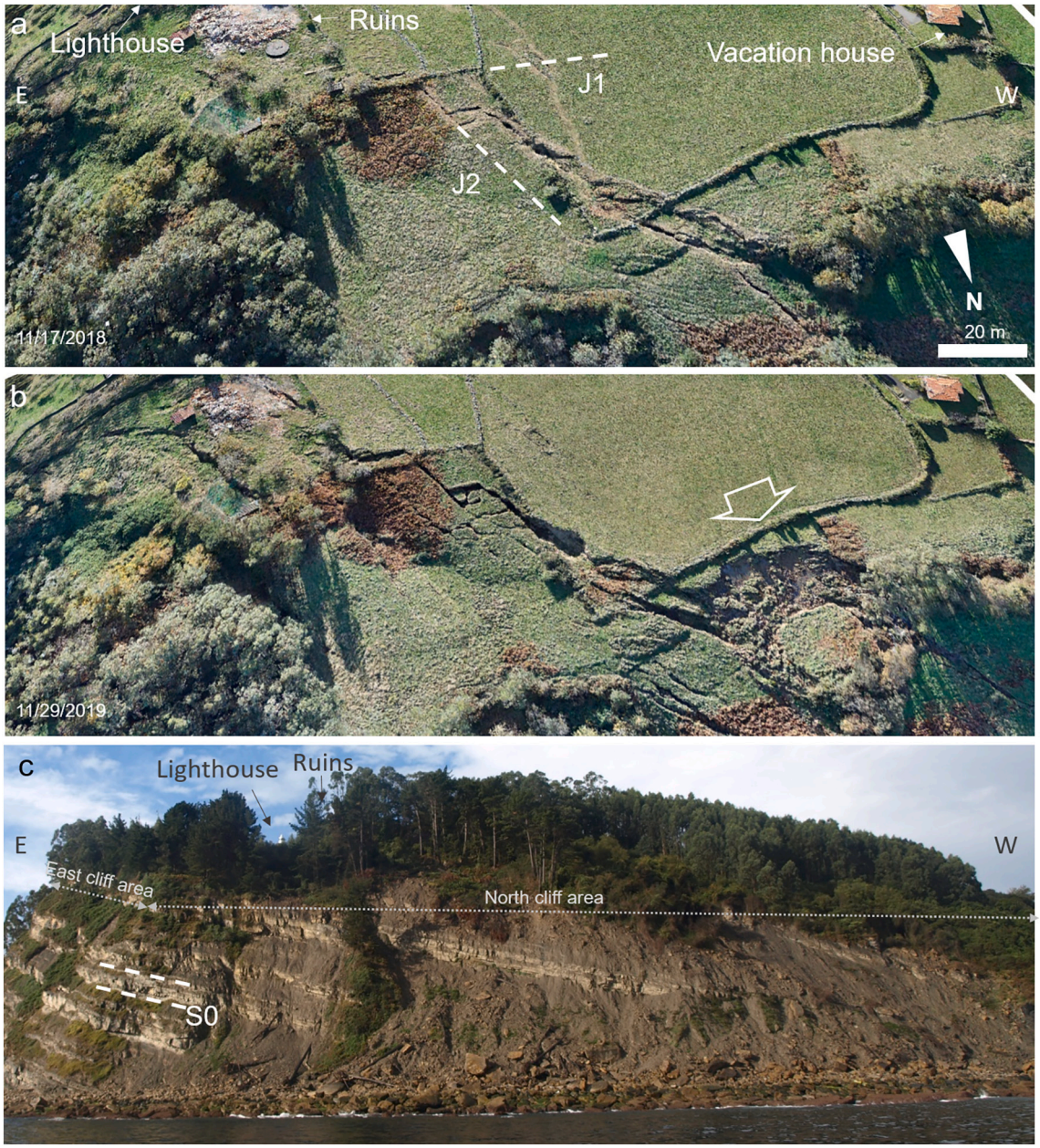

Fig. 5. Tazones Lighthouse slope evolution illustrated on the drone flight imagery of: **a.** 2018 and **b.** 2019. Main families of joints (J1 and J2) are shown. A surficial planar slide is indicated by the arrow. **c.** View of the cliff from the sea showing some detached metric-sized blocks and trees.

predominantly *E*-W to NNE-SSW and NNW-SSE oriented with slopes ranging between 43° and 88°, mainly towards N.

A fluvial network is incised on the *rasa*. Stream courses present predominantly S-N orientations, with longitudinal profiles showing a general slope of 5° (some of them reaching 90° at their mouths), with no evident accumulation of fluvial deposits. With the exception of the stream that flows into Tazones, to the SE of the study area, they are hanging valleys with their mouths located at 25–30 m a.s.l. Slope movements are fundamentally restricted to coastal cliffs, not ruling out the presence of colluviums and small mass movements in river valleys and on other slopes. The main evidence of instabilities corresponds to complex movements affecting the cliffs, separated by more or less clearly marked scars that originate at the boundary between the cliff and the *rasa*. These mass movements mask the mouths of some streams incised on the *rasa*. Marine erosion activity is evidenced by the existence of a scour front, which is present along most of the cliff, and is marked by an area of high slope (70–80°) at its base. At the cliff foot, there are accumulations of deposits, mainly blocks, preserving angular-sub angular particle roundness, although they are partly reworked by the coastal dynamics.

The cliff monitoring area comprises a sector that covers part of the *rasa* bounded by cliffs oriented NW-SE to N-S. Different instabilities have affected this sector and are represented in Fig. 4. These landforms are linked to recent instability evidence marked by fractures and open cracks. To the southeast of the area, associated with the mouth of Los Lindones stream in the Port of Tazones, a set of polygenic forms are located, associated with anthropic, fluvial, gravity and marine origin (Fig. 3).

The most important geomorphological evidence of slope movement in the study area is given by the open cracks, which appear in the upper part of the slope (Figs. 2–5). Our first visit to this area was in February 2018, during the eviction of the restaurant due to the recent appearance of open cracks in the walls that irreversibly affected the structure of the building (Fig. 2a and b). We noticed the presence of old cracks filled with

Table 2
Cumulative displacement measured for each of the 38 markers in the 22 monitoring campaigns.

	3D cumulative displacement (m)																					
Marker	07/11/2018	07/27/2018	10/09/2018	11/19/2018	12/18/2018	01/17/2019	02/15/2019	03/22/2019	04/26/2019	05/24/2019	06/24/2019	07/24/2019	09/20/2019	10/18/2019	11/18/2019	12/12/2019	01/17/2020	02/14/2020	03/13/2020	04/17/2020	05/18/2020	3D Total displacement rank (m)
FG3	0.01	0.03	0.01	0.02	0.01	0.02	0.11	0.13	0.11	0.12	0.10	0.10	0.12	0.10	14.17	14.54	14.89	14.93	15.01	15.06	15.08	10.0 - 16.0
FG1	—	—	—	—	—	0.13	0.98	1.29	1.48	1.54	1.61	1.65	1.72	1.71	2.72	3.61	4.50	4.67	4.87	5.03	5.10	5.0 - 10.0
FF1	—	—	—	—	—	0.13	1.07	1.45	1.67	1.76	1.85	1.88	1.96	1.99	3.20	4.34	5.91	6.60	7.04	7.30	7.34	
FE1	—	—	—	—	—	0.11	0.82	1.06	1.20	1.26	1.29	1.32	1.40	1.41	2.19	2.86	3.56	3.67	3.82	3.97	4.03	4.0 - 5.0
FD1	—	—	—	—	—	0.11	0.80	1.09	1.21	1.26	1.33	1.32	1.40	1.42	2.20	2.90	3.57	3.69	3.83	3.98	4.05	
FH1	—	—	—	—	—	0.10	0.77	0.99	1.13	1.19	1.23	1.25	1.30	1.31	2.18	2.86	3.60	3.73	3.88	3.99	4.06	
FE2	—	—	—	—	—	0.10	0.81	1.08	1.22	1.27	1.33	1.35	1.41	1.43	2.23	2.92	3.62	3.75	3.90	4.05	4.12	
FE3	0.11	0.16	0.25	0.34	—	0.52	1.23	1.48	1.63	1.69	1.74	1.77	1.83	1.84	2.64	3.32	4.01	4.12	4.28	4.41	4.47	
FD3	0.13	0.18	0.26	0.33	0.44	0.53	1.21	1.49	1.61	1.66	1.72	1.74	1.80	1.82	2.64	3.35	4.10	4.23	4.40	4.56	4.63	
FD2	—	—	—	—	—	0.11	0.75	1.04	1.11	1.16	1.21	1.22	1.28	1.29	2.01	2.62	3.21	3.31	3.44	3.56	3.63	3.50 - 4.0
FC1	—	—	—	—	—	0.11	0.76	1.02	1.12	1.17	1.20	1.22	1.28	1.30	2.03	2.64	3.24	3.35	3.48	3.61	3.70	
CAS	—	—	—	—	—	—	—	0.35	0.43	0.53	0.59	0.63	0.69	0.73	1.63	2.46	3.29	3.45	3.65	3.81	3.83	
FG2	0.13	0.16	0.22	0.31	0.37	0.46	1.08	1.26	1.38	1.41	1.44	1.45	1.50	1.51	2.53	3.11	3.65	3.75	3.86	3.93	3.97	
FC2	—	—	—	—	—	0.06	0.51	0.66	0.76	0.78	0.82	0.82	0.86	0.87	1.37	1.74	2.15	2.21	2.30	2.48	2.52	2.50 - 3.50
ARB	—	—	—	—	—	—	—	*0.52*	*0.49*	*0.58*	*0.66*	*0.70*	*0.79*	*0.86*	*2.56*	—	—	—	—	—	—	
FC3	0.10	0.14	0.19	0.25	0.32	0.40	0.88	1.12	1.16	1.19	1.24	1.23	1.28	1.29	1.85	2.34	2.88	2.97	3.10	3.26	3.30	
CA7	—	—	—	—	—	0.09	0.68	0.95	1.02	1.07	1.11	1.15	1.19	1.20	1.89	2.47	3.05	3.17	3.29	3.42	3.46	
FA5	0.08	0.09	0.15	0.19	0.22	0.28	0.61	0.73	0.77	0.79	0.82	0.83	0.85	0.86	1.16	1.39	1.60	1.61	1.66	1.67	1.71	0.50 - 2.50
FA3	0.09	0.09	0.16	0.20	0.26	0.31	0.69	0.77	0.87	0.91	0.93	0.95	0.98	0.97	1.35	1.63	1.89	1.94	2.01	2.04	2.07	
FA9	0.02	0.03	0.04	0.05	0.06	0.07	0.13	—	0.14	0.13	0.14	0.12	0.13	0.13	0.13	0.12	0.12	0.12	0.13	0.12	0.12	0.10 - 0.50
FA1	*0.08*	*0.07*	*0.13*	*0.18*	*0.25*	*0.29*	—	—	—	—	—	—	—	—	—	—	—	—	—	—	—	
FB1	0.02	0.04	0.04	0.04	0.04	0.04	0.06	—	0.05	0.06	0.06	0.05	0.05	0.06	0.06	0.05	0.06	0.06	0.06	0.07	0.06	0.05 - 0.10
FB4	0.02	0.05	0.04	0.04	0.05	0.06	0.07	—	0.07	0.08	0.07	0.05	0.06	0.06	0.06	0.06	0.07	0.07	0.07	0.07	0.06	
CA8	—	—	—	—	—	*0.06*	—	—	—	—	—	—	—	—	—	—	—	—	—	—	—	
FC5	0.01	0.04	0.04	0.05	0.05	0.05	0.07	0.08	0.07	0.08	0.06	0.06	0.07	0.07	0.07	0.06	0.07	0.07	0.07	0.08	0.07	
FC4	0.01	0.05	0.04	0.04	0.07	0.07	0.09	0.09	0.10	0.08	0.08	0.06	0.08	0.06	0.08	0.07	0.08	0.07	0.08	0.09	0.07	
FD4	0.03	0.04	0.04	0.04	0.04	0.06	0.07	—	0.08	0.07	0.07	0.05	0.07	0.08	0.07	0.06	0.08	0.08	0.07	0.07	0.09	
FB2	0.02	0.03	0.04	0.05	0.05	0.07	0.07	0.09	0.09	0.08	0.08	0.08	0.09	0.08	0.08	0.08	0.09	0.09	0.09	0.09	0.09	
FA4	0.02	0.02	0.02	0.01	0.02	0.02	0.03	0.02	0.02	0.02	0.02	0.01	0.01	0.02	0.02	0.01	0.01	0.01	0.01	0.02	0.02	0.0 - 0.05
FB3	0.00	0.02	0.02	0.01	0.02	0.01	0.02	—	0.02	0.02	0.02	0.01	0.02	0.01	0.02	0.01	0.01	0.01	0.02	0.02	0.02	
FA2	0.03	0.01	0.03	0.02	0.03	0.03	0.02	0.02	0.02	0.03	0.04	0.02	0.01	0.03	0.03	0.01	0.01	0.02	0.02	0.02	0.02	
FE4	0.02	0.03	0.01	0.02	0.01	0.03	0.03	0.02	0.03	0.02	0.02	0.01	0.01	0.02	0.03	0.03	0.02	0.02	0.02	0.02	0.02	
FB7	—	—	—	—	—	0.01	0.02	—	0.03	0.03	0.02	0.01	0.01	0.02	0.02	0.01	0.03	0.03	0.03	0.03	0.02	
FA6	0.02	0.01	0.02	0.01	0.01	0.02	0.01	—	0.01	0.02	0.02	0.01	0.02	0.04	0.01	0.01	0.01	0.01	0.01	0.03	0.02	
FA10	0.01	0.00	0.01	0.02	0.02	0.02	0.01	—	0.01	0.01	0.01	0.01	0.03	0.03	0.03	0.02	0.02	0.03	0.03	0.02	0.03	
FB6	0.01	0.02	0.01	0.02	0.02	0.02	0.02	0.02	0.03	0.03	0.01	0.02	0.03	0.02	0.01	0.01	0.02	0.02	0.01	0.02	0.03	
FB5	0.01	0.02	0.02	0.03	0.03	0.04	0.04	—	0.04	—	—	0.03	0.04	0.03	0.03	0.04	0.04	0.04	0.04	0.04	0.04	
FD5	0.02	0.02	0.01	0.01	0.02	0.01	0.02	—	0.02	0.02	0.01	0.05	0.04	0.05	0.04	0.02	0.04	0.03	0.04	0.04	0.05	

Markers: Installed on June 2018 (Bold) and December 2019 (Regular); Lost (Italic).
Hyphen: campaign without measurement. Grey color: the greatest displacements measured between campaigns.

mortar while others showed signs of recent and progressive activity.

In the upper and middle slope sector, there are some cracks, both open and incipient (Fig. 4). The most prominent features in this area are open fissures with a rhomboid morphological pattern, some of which adopt a sigmoid arrangement. On the field, it is possible to distinguish morphologies corresponding to shear and stress cracks. Near the old restaurant, and bordering it to the south and west, the existence of a depressed and flattened area separated by two fractures stands out. The progress of the cracks is shown in Fig. 5a and b. Altogether, the open cracks reach 1282 m in length and the incipient ones 359 m. In addition, some scarps with a total length of 266 m have been mapped in this sector. Towards the west, a large complex mass movement with the individualization of its head and occupying 24.04 m^2 can be seen.

In the cliff sector, there are two well-differentiated areas (Figs. 4 and 5). In the eastern area, the cliff is steep and presents outcrops of layers of the Jurassic substrate, it being possible to distinguish (i) the stratification (S0), (ii) the presence of different joints (J1 or J2) and (iii) four mass movements, two of them incipient ones. The base of the cliff shows an active cliff front due to sea wave undercutting. It delimits an accumulation of blocks (20,863 m^2) reworked by wave action, as evidenced by its morphology and the presence of ridges and grooves arranged obliquely to the coastline. The active cliff front extends for 216 m until it disappears to the north under debris deposited on the beach by gravity. The northern area is characterized by the existence of complex mass movement units, which from SE to NW involve areas with: A) combined action of rockfall, run-off and flow processes; B) combined action of flow and slide processes, and C) predominant action of planar sliding processes, with the presence of cracks normal to the dip direction of the slope, favouring block sliding processes away from the cliff front. A transition zone between gravity and marine processes is defined, lacking

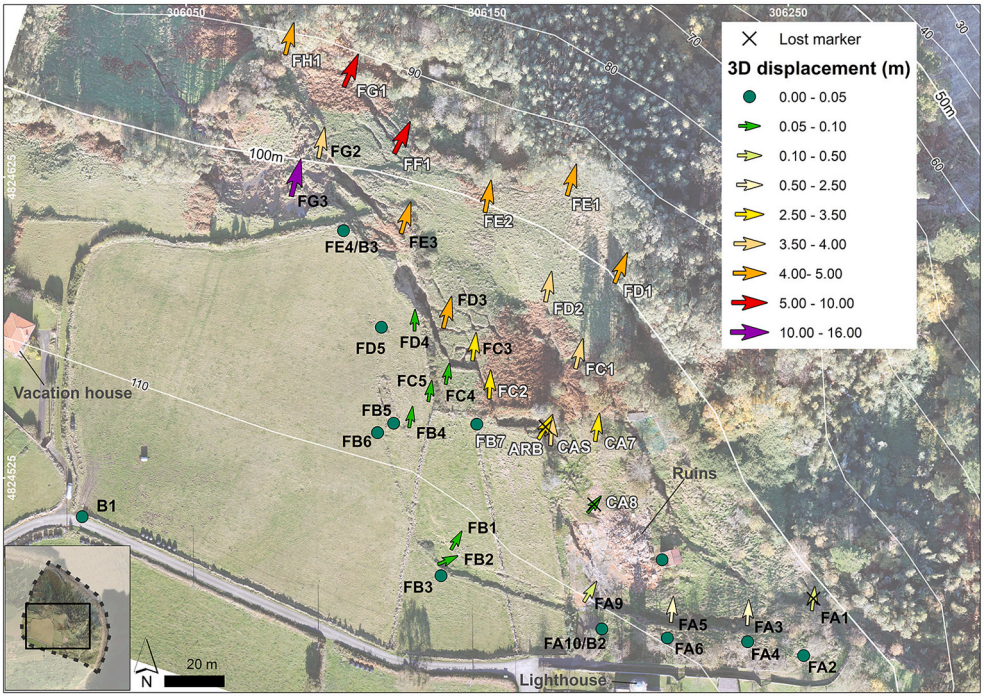

Fig. 6. 3D displacements recorded by 38 markers installed at the Tazones Lighthouse landslide and regularly monitored from June 2018 to May 2020. Arrow size increases proportionally with total displacement values, matching the key color of displacement values compiled in Table 2. Black and white labels refer to markers installed on June and December 2018, respectively. Background image: 2019 drone flight image. UTM coordinates ETRS89, Zone 30.

wave ridge and groove evidence. Various escarpments and displaced masses are observed throughout the cliff sector, which together add up to 602 m of length and 9802 m^2 of surface, respectively. In A, the action of gravity causes the accumulation of debris at the base of the cliff and the appearance of exposed scars, where run-off erosion is clearly visible. There are also some scattered blocks on the slope.

4.2. Slope displacement for the period June 2018–May 2020: Quantitative measurements

The accumulated movements measured in the monitored markers are shown in Table 2 and Fig. 6. The values obtained have been grouped into nine intervals to facilitate their interpretation. Ten markers (FA2, FA4, FA6, FA10, FB3, FB5, FB6, FB7, FD5, FE4), represented by green circles in Fig. 6, are located in zones considered as stable during the observation period. They have accumulated displacements of less than 0.05 cm, which are within measurement uncertainty (< 2 cm). The remaining 28 markers display cumulative movements ranging between 0.06 m (FB1 and FB4) and 15.08 m (FG3) for the period June 12th 2018 to May 18th 2020. The displacement of the monitoring points was uneven in time, with some markers showing evidence of acceleration during the monitoring period, while others shift at regular speed (FB2, FC5). The highest movements observed were recorded on February 2019 (campaign C7) and November 2019 (campaign C15), involving displacements >0.3 m in 16 markers, and > 0.5 m in 12 markers, respectively. The largest 3D displacement was measured during the C15 campaign by marker FG3, which recorded a distance of 14.06 m for the period October–November 2019. Also, another 19 markers moved more than 0.3 m over a single month, four of them reaching metric displacements (ARB = 1.7 m, FF1 = 1.21 m, FG2 = 1.03 m, and FG1 = 1 m).

For instance, FA3 was among the markers that registered the fastest vertical and horizontal displacements for the entire monitoring period, recording shift during every campaign (Fig. 7). This point evidences discontinuous and almost straight movement in the XYZ planes, conditioned by the bedrock bedding as clearly shown by the vertical component. The cumulative 3D monthly displacement recorded by FA3 ranges between 0.01 and 0.38 m.

4.3. Rainfall, soil moisture, wave data and slope displacements

A comparison between the movement measured at 6 markers, rainfall recorded at the permanent meteorological station closest to the landslide, the evolution of soil moisture content and the H_s parameter at SIMAR point 3,098,038 is displayed in Fig. 8 for the surveyed period. For all markers, the largest shifts occurred in January and November 2019. They are indicated by vertical grey bands in Fig. 8. In 2019, two periods of maximum accumulated rainfall were recorded, January–February and October–November. In the first period 646 mm were measured, while in the second 559 mm were reached. The highest daily values were on January 22th and October 19th 2019, when 64.5 and 82.1 mm were recorded, respectively (Fig. 8a). The soil moisture content correlates positively with maximum precipitation values. The soil becomes saturated quickly after the main rainfall peaks, maintaining saturation values higher than 85% for months (Fig. 8c). Regarding the swell, the H_s exceeded 7 m on 4 occasions during the monitoring period, all of them in 2019: March 11th, December 9th, 21st and 22nd December, with heights of 8.35, 7.02, 8.77 and 9.09 m, respectively. Moreover, on January 27th, 2019, an H_s value of 6.54 m is recorded (Fig. 8d) and it should be noted that this was the highest value since March 2014, when a height of 6.56 m had been recorded.

February 2019 is the month that registered the greatest cumulative displacement of the entire survey, with 17 points accumulating between 13 and 49% of the total movement measured for 2 years (Table 3). Exceptional cases are two of these markers, which showed peak movements comprising 93% (FG3) and 66% (ARB) of the total movement measured. Up to this rainfall episode, FG3 had moved less than 1% of the entire measurement period. The displacement observed in February and November 2019 in 20 markers represents between 24% and 94% of the total measured. Likewise, it is noteworthy that 12 of these measurement points were installed on December 2018, despite which they evidence very high movements.

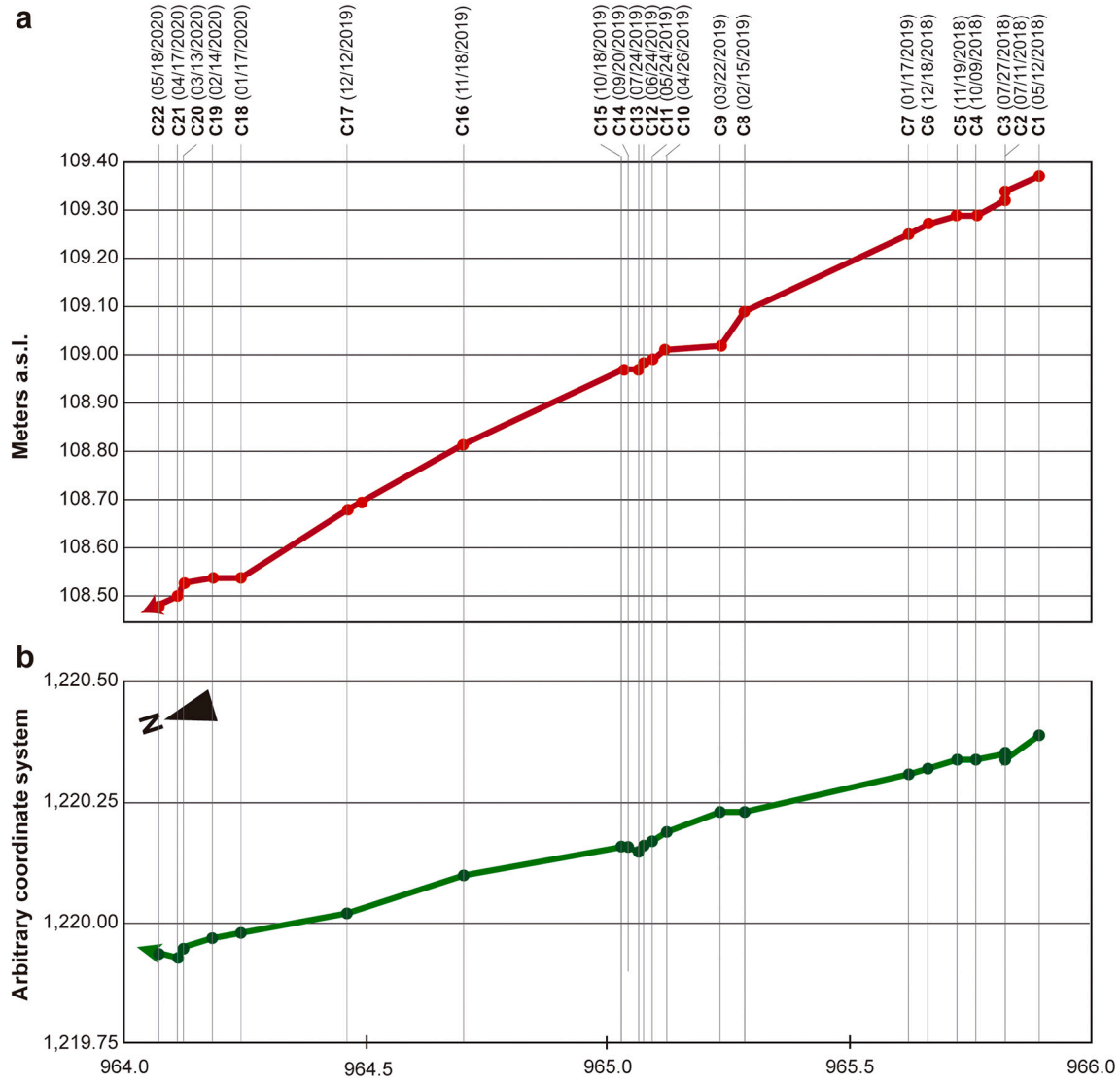

Fig. 7. Time evolution of displacement recorded by marker FA3 over the 22 campaigns. **a.** Vertical (Z) and **b.** planar components of movement.

4.4. Geomechanical features of the bedrock

Three types of bedrock discontinuities have been identified: bedding S0: 002/14, and two joint families J1: 166/75, and J2: 085/89 (Fig. 9). The intersection of these discontinuities facilitates the formation of rocky blocks, whose size depends on the thickness of the layers and the spacing between discontinuities (Figs. 4 and 5c). The main blocks have tabular morphology with size varying between 3 and 9 m. It has been found that the mechanical strength of the Lastres Fm. sandstone decreases drastically when it is weathered. Field tests with a Schmidt hammer gave uniaxial compressive strength values of fresh rock of around 40 MPa. However, although the altered rock maintains a homogeneous and coherent appearance, its strength decreases by more than 50%, which means that it behaves like a weak rock.

4.5. Manual boreholes and water point observations

Five manual boreholes were retrieved from the Quaternary cover overlaying the *rasa* surface, comprising, in the case of F-boreholes, the entire excavated thickness (34, 61 and 101 cm, each). However, for LDP-cores, the recovery did not reach the entire drilled length: 1-LDP, 201/239 cm and 2-LDP, 110/140 cm, respectively (Fig. 10). The presence of humus and pieces of mortar mixed with tiles reveal the anthropogenic influence on the infill sequence, at least in the upper part of the five cores (between 14 and 64 cm, depending on the core, Fig. 10). This is attributed to either agricultural activities or dump infills. Otherwise, the presence of levels of clays with very plastic behaviour is significant. Cohesion values between 29 kPa and 78 kPa and uniaxial compressive strength values between 0.19 and 0.28 MPa have been measured in plastic clays retrieved from LDP-cores. The infiltration rates measured in F-boreholes had values between 5 and 22 mm h^{-1}.

On the other hand, eight water points could be recognized in the field (Fig. 1 and Table 4). Seven of them correspond to active or closed water wells (water points 1 to 7), located in the *rasa* area, and the eighth is a spring in the beach area. The seven wells measured are supply wells in the town of Villar, placed very close to each other over an area of 12,000 m^2. The furthest wells (6 and 7) are 250 m apart. We measured the water table depth in five wells (M in Table 4), which was located at a variable depth of −0.85 to −14.33 m, while the remaining 2 wells were inaccessible, but the owners informed us that the water table was at −32 and −15 m, respectively. Regarding water point 8, it is located very close to the tidal zone, near the base of the cliff (Figs. 1c and 4). Although it was not possible to get eye contact of a water flow, we could clearly hear the distinctive noise of a continuous stream of water falling, sounding similar to a small waterfall. Point 8 has been placed tentatively, as the tidal conditions prevented a precise GPS positioning. Finally, the

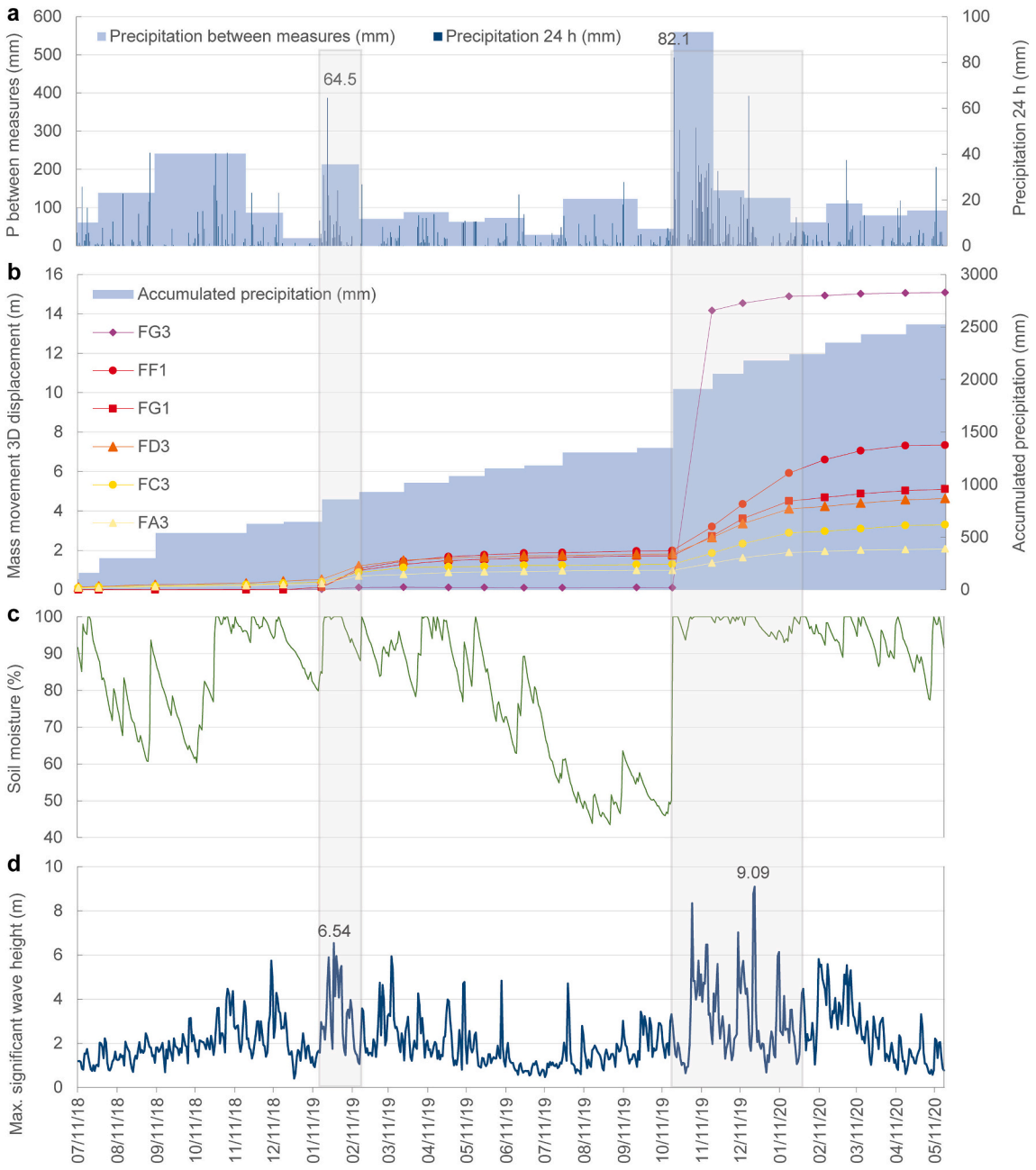

Fig. 8. a. Daily and accumulated rainfall recorded at the Luces-Aspo pluviometer. **b.** Evolution of soil moisture content. **c.** Accumulated rainfall vs. temporal evolution of the 3D displacement of 6 selected markers. **d.** Evolution of the maximum daily H_s at the SIMAR 3098038 point. Source: a–c, AEMET; d, Puertos del Estado. The vertical grey bands indicate the periods with the greatest recorded displacements.

inhabitants of the area informed us about the presence of another potential water point that they place with confidence in the area where the LDP-02 borehole was drilled. They indicate that, on many occasions, "water can be heard roaring under the ground". This could not be verified in the context of our investigation.

5. Discussion

5.1. Characterization of slope instabilities, spatial distribution and conditioning factors

The slope instability is conditioned by a great variety of processes that, according to Varnes (1978), could be classified (on the whole) as a complex landslide. Cliffs show different instability evidence at the northern end of the study area, including blocks, earth and debris deposits, pointing to a complex evolution that combines rock fall, topple, slide and flow processes (Figs. 4 and 5c). Nevertheless, at present, the most outstanding evidence of movement is given by open cracks, whose temporal evolution is shown in Figs. 5a and b and 6. Some of the cracks were already partially visible in the 2001 Google Earth images, and traces of possible cracks can be perceived in aerial photographs since the mid-80s (López-Toyos et al., 2021).

Crack evolution observed over the entire monitored period is closely related to a primary planar landslide following S0 and secondary movements such as flows, topples or rock falls. Topographic factors (slope and height), together with structural and lithological factors, as well as marine and anthropogenic action, are the main conditioning factors of instability, as we will discuss in the following paragraphs. The height of the cliff is a critical factor conditioning cliff retreat. The geomorphological study has indicated the scars of ancient mass

Table 3
Displacement measured for the 20 most active markers in the January–February 2019 (C6–C7) and October–November 2019 (C14–C15) monitoring campaigns.

	Feb - Jan 2019 3D displacement				Nov - Oct 2019 3D displacement				Feb + Nov 2019		
	m				m				m	%	
Marker	01/17/2019	02/15/2019	Feb - Jan 2019	%	10/18/2019	11/18/2019	Oct - Nov 2019	%	3D displacement	3D displacement	Total 3D displacement rank (m)
FG3	0.02	0.11	0.10	0.66	0.10	14.17	14.06	93.25	15.08	93.91	10.0 - 16.0
FG1	0.13	0.98	0.85	16.67	1.71	2.72	1.00	19.61	5.10	36.28	5.0 - 10.0
FF1	0.13	1.07	0.94	12.81	1.99	3.20	1.21	16.48	7.34	29.29	
FE1	0.11	0.82	0.71	17.60	1.41	2.19	0.78	19.33	4.03	36.93	4.0 - 5.0
FD1	0.11	0.80	0.70	17.29	1.42	2.20	0.78	19.26	4.05	36.55	
FH1	0.10	0.77	0.67	16.50	1.31	2.18	0.87	21.42	4.06	37.92	
FE2	0.10	0.81	0.71	17.24	1.43	2.23	0.80	19.43	4.12	36.67	
FE3	0.52	1.23	0.71	15.87	1.84	2.64	0.80	17.88	4.47	33.74	
FD3	0.53	1.21	0.68	14.69	1.82	2.64	0.82	17.72	4.63	32.41	
FD2	0.11	0.75	0.64	17.62	1.29	2.01	0.72	19.82	3.63	37.44	3.50 - 4.0
FC1	0.11	0.76	0.66	17.84	1.30	2.03	0.73	19.73	3.70	37.57	
CAS	—	—	—	0.00	0.73	1.63	0.90	23.53	3.83	23.53	
FG2	0.46	1.08	0.61	15.38	1.51	2.53	1.03	25.97	3.97	41.35	
FC2	0.06	0.51	0.45	17.87	0.87	1.37	0.50	19.85	2.52	37.72	2.50 - 3.50
ARB	—	—	—	*0.00*	*0.86*	*2.56*	*1.70*	*66.48*	*1.00*	*66.48*	
FC3	0.40	0.88	0.49	14.84	1.29	1.85	0.56	16.96	3.30	31.79	
CA7	0.09	0.68	0.59	17.03	1.20	1.89	0.69	19.92	3.46	36.95	
FA5	0.28	0.61	0.33	19.31	0.86	1.16	0.30	17.55	1.71	36.86	0.50 - 2.50
FA3	0.31	0.69	0.38	18.33	0.97	1.35	0.38	18.33	2.07	36.66	
FA9	0.07	0.13	0.06	48.76	0.13	0.13	0.00	0.00	0.12	48.76	0.10 - 0.50

Markers: Installed on June 2018 (Bold) and December 2019 (Regular); Lost (Italic).

movements along the Jurassic Cantabrian Coast (Fig. 3) that reach 120 m in height. High cliffs are more prone to break in favour of bedrock discontinuities, as previous authors have documented (Sunamura, 1992; Colantoni et al., 2004; Matano et al., 2015; He et al., 2022). In this regard, ancient scars in the study area have similar dimensions and characteristics to recent ones observed in the Tazones Lighthouse area, suggesting that voluminous mass movements are fundamental in the long term evolution of the Asturian Jurassic coast.

Marine erosion is evidenced by the presence of a scour front at the cliff foot in some sectors of the study area. Stormy waves (the most energetic ones) in this reach of the coastline frequently come from the northwest (Izaguirre et al., 2011) and thus, considering the orientation of the coast in the studied section, the toe of the unstable slope is exposed to their direct impact. Otherwise, the coastal drift in this area comes from the West, so the Tazones Port groyne, located east of the study cliff (Fig. 1b), does not play a fundamental role.

The analysis of the geomorphological evidence in the surroundings of the Tazones Lighthouse, suggests that the cliff retreat is faster than the fluvial incision due to the presence of hanging valleys whose streams flow over the cliffs to the sea. Regarding the cliff retreat, field observations and photographic analysis suggest that it occurs episodically, as evidenced by the cracks already present in the 2001 photographs and by the acceleration episodes identified during the monitoring. This is in line with observations by Costa et al. (2019), who indicate that cliff evolution occurs on time scales ranging from 10 to 70 years depending on bedrock lithology. Although crack opening has accelerated over the study period, hillside material is slowly being released in the surroundings of the Tazones Lighthouse without entailing a sudden voluminous disaggregation of bedrock materials at the base of the cliff yet. The presence of well-developed bedding and two families of discontinuities, with an average spacing ranging between 20 and 60 cm (Fig. 9a and b), favour the individualization of decametric to metric sandstone blocks, instead of a large slip.

The combination of bedding alternations of different lithology, the disposition of bedding (S0) planes and the presence of two family joints offers altogether a situation that favours slope movement. The displacement vectors are mostly oriented to N-NNE and NE (Fig. 6), pointing to a direction of movement consistent with the dip angle of bedding planes (S0: 002/14), which are favourably oriented towards the cliff. In fact, the orientation of the coast with respect to discontinuities (S0, J1, and J2) and their spacing has conditioned the evolution of the Tazones Lighthouse slope, as previously reported in other areas like the North Coast of Cornwall in the UK (Francioni et al., 2018). Thus, a translational slide involving soil and bedrock was initiated using S0 as the rupture surface in November 2019 (Fig. 9e). Also, the vertical movement of the FA3 marker approaches the dipping angle of S0 (15–17°N; Fig. 7). The close relationship between crack trends and the position of joint families (J1 and J2) is shown in Fig. 9.

Regarding weathering processes, the Lastres Formation (sandstone beds) reacts with slightly acid meteoric water that infiltrates through joints, causing dissolution of the ferrous calcite cement (García-Ramos, 2013). This process progresses relatively quickly and gives rise to a variable thickness of very porous sandstone with remains of quartz cement. Pores quickly saturate during rainfall periods, promoting an important increase in weight of the sandstone blocks and their consequent sliding along bedding planes. Moreover, marl beds probably work as slipping planes due to their plastic (ductile) behaviour once saturated. A translational slip involving displacement of the FG3 marker occurred after a rainy period in November 2019, exemplifying this control. The metastable block where FG3 was installed lies on a layer of marl that accumulated notable displacement during that event (Fig. 9e). We consider that this small-scale example is illustrative of what is

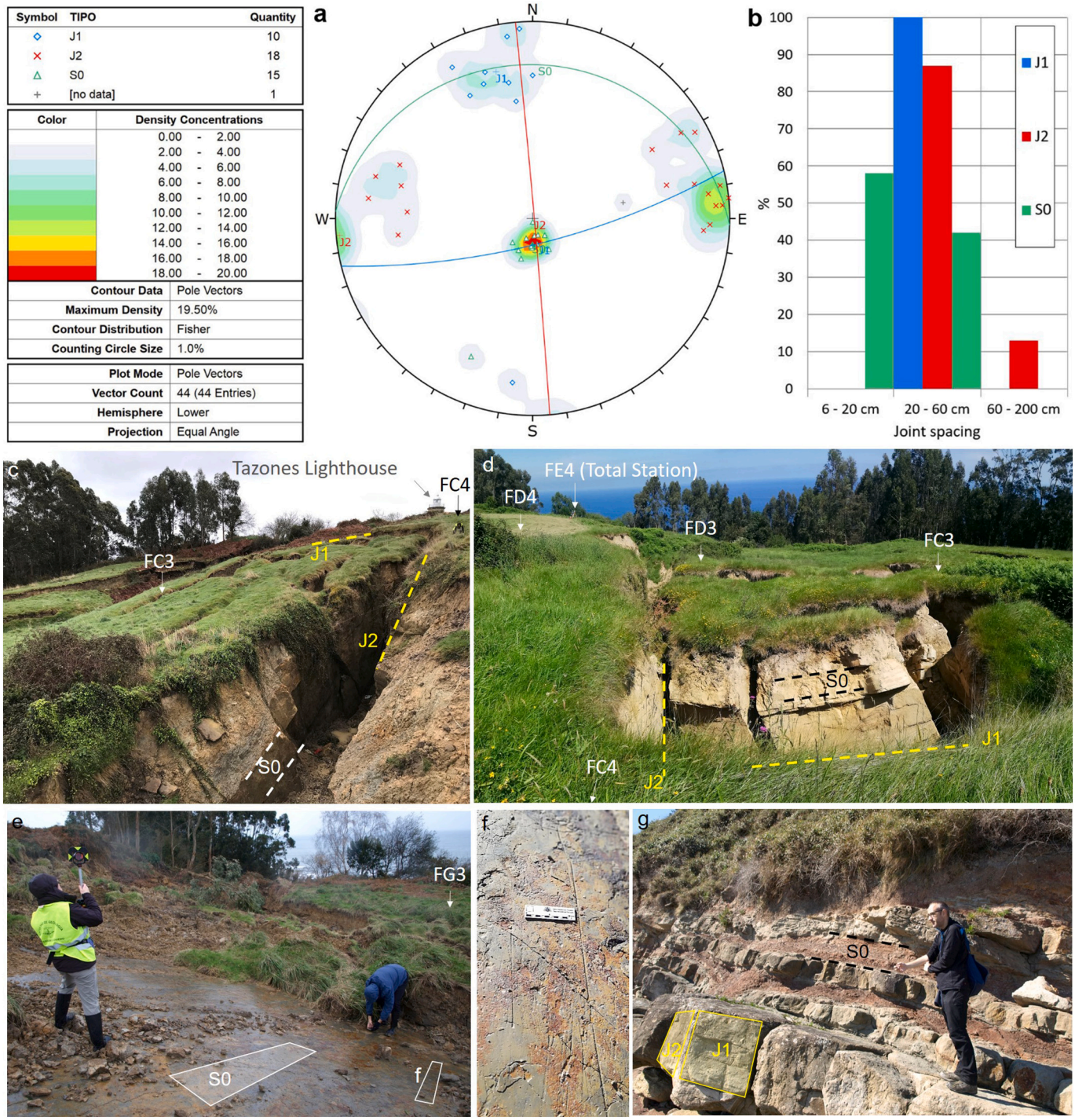

Fig. 9. a. b. Stereographic projection of the discontinuities measured in the bedrock and median planes corresponding to the identified families of discontinuities. **c. d.** Two views of the central part of the monitored area (FC2–FC5 area), showing S0 and J1–J2 family joints and the position of some markers. **e.** Surficial slide occurred in November 2019. **f.** Detail of the grooves marked in the bedrock marl layer after the surficial slide occurrence. **g.** Bedrock detail showing S0 and J1–J2 family joints at the foot of the cliff.

happening on the entire slope.

Is noteworthy that previous studies describe some lineal hollows in the area as jet-black mining gallery collapses (Crespo et al., 2008). However, we have not found unequivocal evidence of abandoned mining galleries within the study area during the numerous and exhaustive field work campaigns and, hence, the role of abandoned galleries in promoting slope instability initiation remains undetermined.

5.2. Relationships between the current evolution of displacement and waves and rainfall

The open and incipient cracks reach a total cumulative length of 1641 m, a maximum depth of 10 m and 8 m of maximum width. They can be perceived in 2001 Google Earth images and have been clearly visible since 2016. At the time of writing, cracks continue to grow due to slope activity.

The temporal coincidence between precipitation, soil moisture

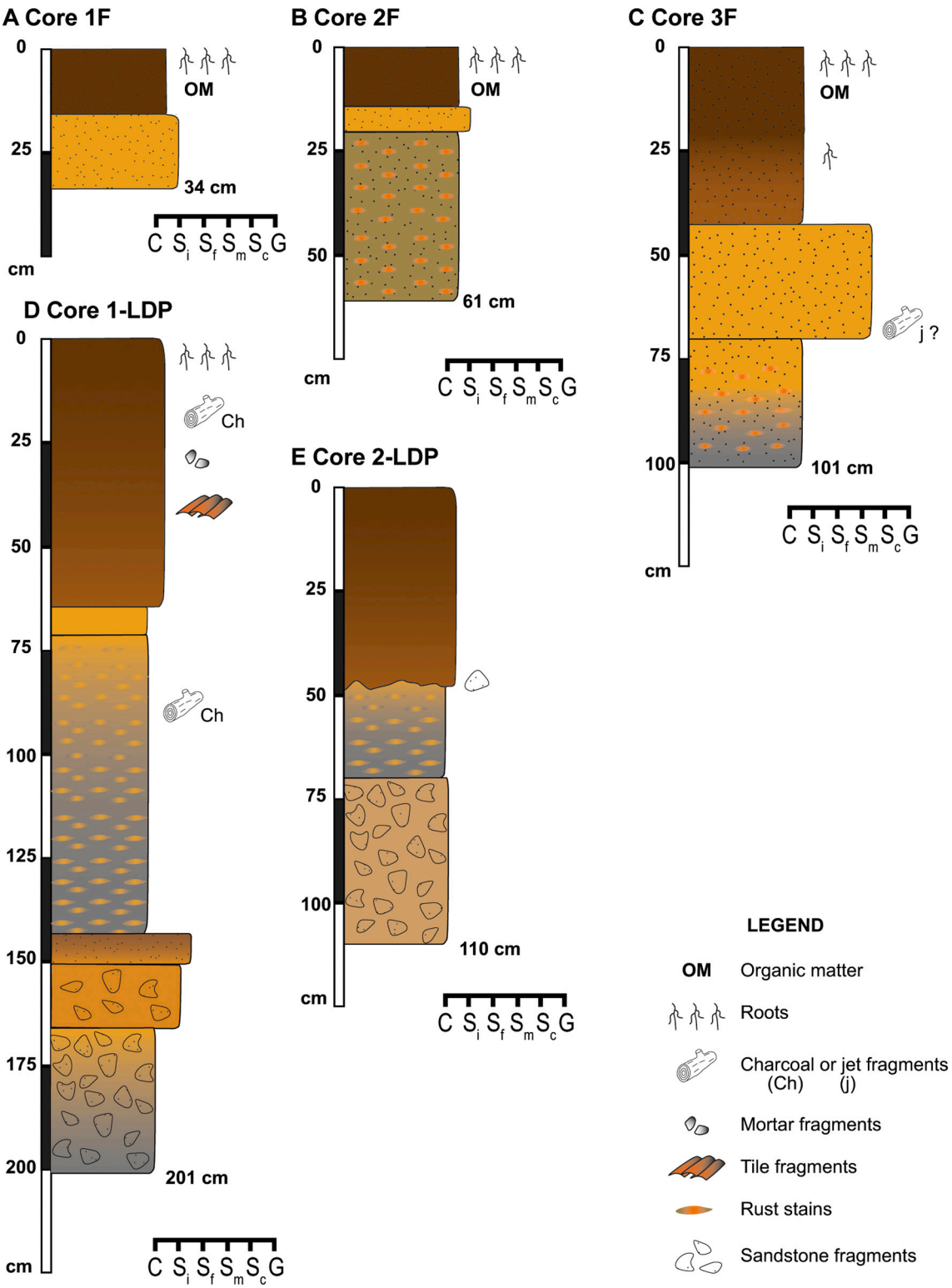

Fig. 10. Stratigraphic columns of F-01, F-02, F-03, LDP-01 and LDP-02 sediment cores (C – clay; Si – silt; S_f – fine sand; S_m – sand medium; S_c – sand coarse; G – gravel). Borehole locations are shown in Fig. 1.

saturation, H_s and crack opening and progression has been verified, as shown in Fig. 8. However, since only monthly marker movement data are available, it is not possible to discern whether point accelerations are more closely related to waves or to precipitation and soil saturation. To clarify this it would be necessary to have a longer monitoring period and with more detailed data, which would allow a daily analysis of slope movement events. In any case, the analysis of the historical data at SIMAR point 3,098,038 shows that, in recent times, the events with extreme H_s values have been far more numerous. Thus, between January 1st, 1960 and December 31st, 2020, there have been 35 events with $H_s \geq 5.90$ m, 54% of them concentrated in the last decade, suggesting an increase in storm strength, with $H_s > 8.0$ m being more frequent since 2014, leading to enhanced storm wave erosion capacity and significant erosion of dune coastlines in the region (Flor-Blanco et al., 2021). In the

Table 4
Summary of water point observations.

Water point	Type: well (W) or spring (S)	Depth of water from ground surface (m)	Measured (M)/ or estimated (E)	Surface level (m)	Water level (m)
1	W	14.33	M	122.10	107.77
2	W	5.60	M	121.05	115.45
3	W	3.57	M	120.25	116.68
4	W	0.85	M	127.90	127.05
5	W	32.00	E	122.68	90.68
6	W	4.65	M	128.68	124.03
7	W	15.00	E	120.14	105.14
8	S	0.50	E	2.74	2.24

last 40 years only 12 events have shown $H_s > 7.0$ m at SIMAR point 3,098,038, and four (one third) took place after January 2018. All this could justify the acceleration of the Tazones Lighthouse landslide movement in recent times and its relationship with both marine and continental factors.

The cross-comparison between climatic and wave series and the displacement recorded for the studied period shows a positive correlation, with increasing displacement when soil moisture content increases in response to rainfall episodes. Two events of accelerated displacement have been recognized, conspicuously recorded by markers FG1, FF1, and FG3. The most important displacements were registered during the periods January–April 2019 and October 2019–March 2020, coinciding with soil moisture content values that were above 90% for most of the time (Fig. 8). Between January and May 2020, markers FC3, FD3, FG1, and FF1 registered another displacement episode after the second rainfall peak, followed by a gradual reduction until April 2020. In contrast, the movement was almost inappreciable during May.

The evolution of FC3, FD3, FG1, and FF1 markers in 2020 reveals the close relationship between sliding activation and soil moisture. Accumulated precipitation marked a stable trend during 2020 (Fig. 8), but a reduction in daily rainfall and an increase in the length of dry periods were observed. This fact, together with the seasonal increase in evapotranspiration, explains the gradual decrease in soil moisture content to values under 90%. Hence, the change to an under-saturated soil condition may correlate with the drastic displacement reduction.

The temporal evolution of recorded displacements registered for the most active markers highlights the episodic character of sliding activity, conditioned by the occurrence of rainfall events long or intense enough to produce a sudden rise of soil moisture content surpassing values of 90% and sustained over weeks or months, and their temporal coincidence with sea storms with H_s peaking around 6 m or more. The use of the AWC index to represent the evolution of soil moisture content has some limitations, as it is calculated considering the behaviour of a soil of a given thickness. However, most of the unstable mass is composed of bedrock materials and hence, water infiltration through crack systems, which feeds the rupture surface, may also play a significant role in displacement modulation. Moreover, the weathering processes affecting the Lastres Fm. caused an important increase in porosity, so the AWC index could be used to estimate water pore saturation linked to peaks in rainfall. Thus, the evolution of displacement could be controlled by the weight increase of bedrock blocks as their pores become saturated with water, more than by the daily rainfall, since the evolution of soil moisture content is also controlled by other factors, such as the antecedent soil moisture conditions or changes in soil temperature.

Alternations, in space and time, of subaerial and marine action in the cliffs of the study area seem to occur, as has been described in cliffs in Galicia (Gómez-Pazo et al., 2021). Precipitation events often coincide with periods of higher waves, which promote wave quarrying and cliff undermining, eventually conducing to cliff destabilization and removal of talus deposits that had been buttressing the foot of the cliff. The accumulation of a mixture of blocks, gravel and fine material in some areas of the study area reflects time lapses with higher geomorphological activity linked to gravity processes rather than to littoral activity (López-Toyos et al., 2021). This study showcases the close relationship between rainfall and slope movement episodes. Precipitation and soil moisture content determine cliff instability as has been shown in other rocky coastal areas (Young et al., 2009). However, the cross comparison of wave height records and sea storm episodes with sliding acceleration events also suggest straightforward relationships, as displacement acceleration occurs when sea storms and rainfall events coincide.

6. Conclusions

The design and application of a high resolution multidisciplinary work methodology to develop a 4d model of an active cliff on the Jurassic Coast (Tazones Lighthouse), has allowed a substantial advance in the understanding of the progress of the retreat of the Cantabrian Coast in Northern Spain in spatial and temporal terms. This is based on the points listed below, responding to the aims of the work.

- The Tazones cliff shows the importance of the contribution of slope instability processes summarized by the presence of a complex mass movement with a primary planar landslide type, with secondary movements such as flows, topples or rock falls.
- From a quantitative point of view, from 2018 to 2020, the spatial and temporal activity of the gravity processes is evidenced by the progressive opening of cracks, and significant displacements of topographic markers, moving more than 1 m and even exceeding 15 m of displacement.
- The conditioning factors of the slope evolution include: 1) bedrock lithology (weathered alternation of marl, limestone and sandstone); 2) bedrock structure, including the bedding observed in the marl layers (S0, 360/15–17) and the progressive opening of conjugated tension cracks related to two joint families: (J1 and J2, dipping respectively 262/85 and 166/75); and 3) the topography and geomorphological history, including the development of sea undercutting at the foot of the cliff.
- The main triggering factors controlling planar sliding are linked to variation in precipitation and soil moisture content, as proved by the good correlation between them: the greatest displacements occurred after 2 periods of heavy rain in January and October–November 2019, also coeval with sea storms with Hs $\geq$ 6.5 m.
- Finally, this research indicates the contribution of gravity processes to the dynamics of the Cantabrian coastal cliffs, combining geological factors (bedrock lithology and structure), geomorphological factors (topography and sea erosion), together with climatic factors (rainfall and soil moisture). The monitoring period should be extended in time to confirm these relationships. In addition, this study improves the understanding of the complex set of mechanisms involved in the evolution of rocky coast retreat and provides essential data for future prediction models.

Declaration of Competing Interest

The authors declare that they have no known conflicts of interest that could influence the work presented in this article.

Acknowledgments

This research is part of 1) the “COSINES” Project [CGL2017-83909-R], Call 2017 for RETOS Projects funded by the Spanish Economy, Industry and Competitiveness Ministry-Ministerio de Economía, Industria y Competitividad (MINECO), the Spanish Research Agency-Agencia Estatal de Investigación (AEI) and the European Regional Development Found (FEDER) and 2) the GEOCANCOSTA research group, supported by the Asturian Regional Government (Spain) [grant number GRUPIN-IDI-2018-184].

The authors thank José Carlos García-Ramos and Laura Piñuela of MUJA for accompanying us on some field trips and sharing their knowledge about the Lastres Fm.; Carlos Espadas of INGECOR GEOMÁTICA for the drone flights; and the City Council and Civil Protection of the Villaviciosa municipality for the opportunity provided to analyse the cliff from a boat from the sea.

The review work of two anonymous referees is gratefully acknowledged. In addition, we thank Alan Trenhaile for his detailed and constructive review of an earlier version of this manuscript.

References

Avanzini, M., Piñuela, L., García-Ramos, J.C., 2010. First report of a Late Jurassic lizard-like footprint (Asturias, Spain). J. Iber. Geol. 36, 175–180. https://doi.org/10.5209/rev_JIGE.2010.v36.n2.5.

Badenas, B., Aurell, M., Armendariz, M., Rosales, I., García-Ramos, J.C., Piñuela, L., 2012. Sedimentary and chemostratigraphic record of climatic cycles in Lower Pliensbachian marl-limestone platform successions of Asturias (North Spain). Sediment. Geol. 281, 119–138. https://doi.org/10.1016/j.sedgeo.2012.08.010.

Bahamonde, J., Cossio, J., Muñoz de la Nava, P., Cembranos, V., 1986. Posibilidades de Azabaches en Asturias. IGME, Madrid.

Blanco-Chao, R., Pérez-Alberti, A., Trenhaile, A.S., Costa-Casais, A., Valcarcel-Díaz, M., 2007. Shore platform abrasion in a para-periglacial environment, Galicia, northwestern Spain. Geomorphology 83, 316–331. https://doi.org/10.1016/j.geomorph.2006.06.028.

BOE, 2014. https://www.boe.es/boe/dias/2014/04/23/pdfs/BOE-B-2014-14482.pdf.

Botey, R., Moreno, J., 2012. Metodología para estimar la humedad del suelo mediante un balance hídrico exponencial diario (Balance hídrico 2). AEMET, Madrid.

Castedo, R., Fernández, M., Trenhaile, A.S., Paredes, C., 2013. Modeling cyclic recession of cohesive clay coasts: effects of wave erosion and bluff stability. Mar. Geol. 335, 162–176. https://doi.org/10.1016/j.margeo.2012.11.001.

Colantoni, P., Mencucci, D., Nesci, O., 2004. Coastal processes and cliff recession between Gabicce and Pesaro (northern Adriatic Sea): a case history. Geomorphology 62, 257–268. https://doi.org/10.1016/j.geomorph.2004.03.003.

Costa, S., Maquaire, O., Letortu, P., Thirard, G., Compain, V., Roulland, T., Medjkane, M., Davidson, R., Graff, K., Lissak, C., Delacourt, C., Duguet, T., Fauchard, C., Antoine, R., 2019. Sedimentary coastal cliffs of normandy: modalities and quantification of retreat. In: Castelle, B., Chaumillon, E. (Eds.), Coastal Evolution under Climate Change along the Tropical Overseas and Temperate Metropolitan France. J. Coast. Res. 88, Coconut Creek, Florida, pp. 46–60. https://doi.org/10.2112/SI88-005.1.

Crespo, S., Sierra, M., Fernández, S., Herrera, D., 2008. Plan Especial de Protección y Rehabilitación de Tazones-Villaviciosa. Ayuntamiento de Villaviciosa.

De Sanjosé Blasco, J.J., Gómez-Lende, M., Sánchez-Fernández, M., Serrano-Cañadas, E., 2018. Monitoring retreat of coastal sandy systems using geomatics techniques: Somo Beach (Cantabrian Coast, Spain, 1875-2017). Remote Sens. 10, 1500. https://doi.org/10.3390/rs10091500.

Del Río, L., Gracia, F.J., 2009. Erosion risk assessment of active coastal cliffs in temperate environments. Geomorphology 112, 82–95. https://doi.org/10.1016/j.geomorph.2009.05.009.

Domínguez-Cuesta, M.J., Jiménez-Sánchez, M., González-Fernández, J.A., Quintana, L., Flor, G., Flor-Blanco, G., 2015. GIS as a tool to detect flat erosional surfaces in coastal areas: a case study in North Spain. Geol. Acta 13, 97–106. https://doi.org/10.1344/GeologicaActa2015.13.2.2.

Domínguez-Cuesta, M.J., Valenzuela, P., Jiménez-Sánchez, M., Rodríguez-Rodríguez, L., Ballesteros, D., 2018a. Slope Instabilities in the Asturian Coast (N of Iberian Peninsula): A Preliminary Overview. EGU General Assembly, Vienna, Austria, 8–13 April 2018, EGU2018–13525.

Domínguez-Cuesta, M.J., Valenzuela, P., Rodríguez-Rodríguez, L., Ballesteros, D., Jiménez-Sánchez, M., Piñuela, L., García-Ramos, J.C., 2018b. Cliff coast of Asturias. In: Morales, J.A. (Ed.), The Spanish Coastal Systems, Dynamic Processes, Sediments and Management. Springer, Berlin, Heidelberg, pp. 49–77. https://doi.org/10.1007/978-3-319-93169-23.

Domínguez-Cuesta, M.J., López-Fernández, C., González-Pumariega, P., Valenzuela, P., Marigil, M.A., Jiménez-Sánchez, M., Mora, M., Ballesteros, D., Rodríguez-Rodríguez, L., Pando, L., Meléndez, M., Flor, G., Espadas, C., Zêzere, J.L., Oliveira, S. C., Alcántara, J., Bobrowsky, P., 2019. Slope Instability as a Proxy of Cantabrian Coast Retreat (N Iberia): A Multidisciplinary Approach. EGU General Assembly, Vienna, Austria, 7–12 April 2019, EGU2019–9729-1.

Domínguez-Cuesta, M.J., Ferrer Serrano, A., Rodríguez-Rodríguez, L., López-Fernández, C., Jiménez-Sánchez, M., 2020a. Analysis of the Cantabrian Coast retreat around the Peñas Cape (Asturias, N Spain). Geogaceta 68, 63–66.

Domínguez-Cuesta, M.J., González-Pumariega, P., Valenzuela, P., López-Fernández, C., Herrera, F., Mora, M., Meléndez, M., Marigil, M.A., Espadas, C., Cuervas-Mons, J., Pando, L., Jiménez-Sánchez, M., 2020b. The Fast Evolution of the Tazones Lighthouse Landslide (N Spain): Multidisciplinary 3D Monitoring between 2018 and 2019. EGU General Assembly. Online, 4–8 May 2020, EGU2020–10175.

Duguet, T., Duperret, A., Costa, S., Regard, V., Maillet, G., 2021. Coastal chalk cliff retreat rates during the Holocene, inferred from submarine platform morphology and cosmogenic exposure along the Normandy coast (NW France). Mar. Geol. 433, 106405. https://doi.org/10.1016/j.margeo.2020.106405.

EUROSION, 2004. Living with Coastal Erosion in Europe: Sediment and Space for Sustainability: Part I – Major Findings and Policy Recommendations of the EUROSION Project. European Commission, Directorate General Environment, Brussels.

Flor, G., Flor-Blanco, G., 2005. An introduction to the erosion and sedimentation problems in the coastal regions of Asturias and Cantabria (NW Spain) and its implications on environmental management. J. Coast. Res. 49, 58–63.

Flor-Blanco, G., Alcántara-Carrió, J., Jackson, D.W.T., Flor, G., Flores-Soriano, C., 2021. Coastal erosion in NW Spain: recent patterns under extreme storm wave events. Geomorphology 387, 107767. https://doi.org/10.1016/j.geomorph.2021.107767.

Francioni, M., Coggan, J., Eyre, M., Stead, D., 2018. A combined field/remote sensing approach for characterizing landslide risk in coastal areas. Int. J. Appl. Earth Obs. Geoinf. 67, 79–95. https://doi.org/10.1016/j.jag.2017.12.016.

García Couto, M.A., 2011. Iberian Climate Atlas. AEMET (España) and Instituto de Meteorología (Portugal), Madrid.

García-Ramos, J.C., 2013. El Jurásico de la costa centro-oriental de Asturias. Un Monumento Natural de alto interés patrimonial, VII Jornadas de Geomorfología Litoral, Geotemas, Oviedo, Spain, 13–17 July 2013, pp. 19–29.

García-Ramos, J.C., Aramburu, C., 2010. Las sucesiones litorales y marinas del Jurásico Superior. Acantilados de Tereñes (Ribadesella) y de la playa de La Griega (Colunga), Guía de campo (excursión B). V Congreso del Jurásico de España, Colunga.

García-Ramos, J.C., Gutiérrez Claverol, M., 1995. La cobertera mesozoico-terciaria. In: Aramburu, C., Bastida, F. (Eds.), Geología de Asturias. Trea, Gijón, pp. 81–94.

Gómez-Pazo, A., Pérez-Alberti, A., Trenhaile, A., 2021. Tracking the behavior of rocky coastal cliffs in northwestern Spain. Environ. Earth Sci. 80, 757. https://doi.org/10.1007/s12665-021-09929-4.

He, L., Coggan, J., Stead, D., Francioni, M., Eyre, M., 2022. Modelling discontinuity control on the development of Hell's Mouth landslide. Landslides 19, 277–295. https://doi.org/10.1007/s10346-021-01813-3.

IGN-Instituto Geográfico Nacional, 2006. Corine land cover. In: European Commission Programme to Coordinate Information on the Environment (accessed 25 January 2021).

Isaev, V.S., Koshurnikov, A.V., Pogorelov, A., Amangurov, R.M., Podchasov, O., Sergeev, D.O., Buldovich, S.N., Aleksyutina, D.M., Grishakina, E.A., Kioka, A., 2019. Cliff retreat of permafrost coast in south-west Baydaratskaya Bay, Kara Sea, during 2005–2016. Permafr. Periglac. Process. 30, 35–47. https://doi.org/10.1002/ppp.1993.

Izaguirre, C., Méndez, F.J., Menéndez, M., Losada, I.J., 2011. Global extreme wave height variability based on satellite data. Geophys. Res. Lett. 38, L10607. https://doi.org/10.1029/2011GL047302.

Jongejan, R., Ranasinghe, R., Wainwright, D., Callaghan, D.P., Reyns, J., 2016. Drawing the line on coastline recession risk. Ocean Coast. Manag. 122, 87–94. https://doi.org/10.1016/j.ocecoaman.2016.01.006.

Kamp, U., Owen, L.A., 2022. Polygenetic landscapes: approaches and concepts. In: Shroder, J.J.F. (Ed.), Treatise on Geomorphology 2, Second edition. Academic Press, Cambridge, pp. 749–784.

Kennedy, D.A., Stephenson, W.J., Naylor, L.A. (Eds.), 2014. Rock Coast Geomorphology: A Global Synthesis. Geological Society Books, London.

Knight, J., Mitchell, W.A., Rose, J., 2011. Geomorphological field mapping. In: Smith, M. J., Paron, P., Griffiths, J.S. (Eds.), Developments in Earth Surface Processes, 15. Elsevier, Amsterdam, pp. 151–187.

López, M.T., 2012. Mapa de rocas y minerales industriales de Asturias. Escala 1:200.000. IGME, Madrid.

López-Toyos, L., Domínguez-Cuesta, M.J., Piñuela, L., 2021. Gravity processes and palaeontological discoveries on the Dinosaur Coast (Asturias, N Spain). Geogaceta 69, 1–4.

Matano, F., Pignalosa, A., Marino, E., Esposito, G., Caccavale, M., Caputo, T., Sacchi, M., Somma, R., Troise, C., De Natale, G., 2015. Laser scanning application for geostructural analysis of tuffaceous coastal cliffs: the case of Punta Epitaffio, Pozzuoli Bay, Italy. Eur. J. Remote Sens. 48, 615–637. https://doi.org/10.5721/EuJRS20154834.

Merino Tomé, O., Suárez Rodríguez, A., Alonso, J.L., 2013. Mapa Geológico Digital continuo de España 1:50.000, Zona Cantábrica (Zona-1000), GEODE. https://igme.maps.arcgis.com/home/webmap/viewer.html?webmap=44df600f5c6241b59edb596f54388ae4/ (accessed 25 February 2021).

MITECO-Ministerio para la Transición Ecológica y el Reto Demográfico, 2021. Inversiones en Asturias. https://www.miteco.gob.es/en/costas/temas/proteccion-costa/actuaciones-proteccion-costa/asturias/actuaciones-asturias-gijon.aspx/ (accessed 27 September 2021).

Monte Carreño, V., 2004. El azabache. In: Piedra mágica, joya, emblema jacobeo. Gijón, Editorial Picu Urriellu.

Morales, T., Clemente, J.A., Damas Mollá, L., Izagirre, E., Uriarte, J.A., 2021. Analysis of instabilities in the Basque Coast Geopark coastal cliffs for its environmentally friendly management (Basque-Cantabrian basin, northern Spain). Eng. Geol. 283, 106023. https://doi.org/10.1016/j.enggeo.2021.106023.

Mushkin, A., Katz, O., Porat, N., 2019. Overestimation of short-term coastal cliff retreat rates in the eastern Mediterranean resolved with a sediment budget approach. Earth Surf. Process. Landf. 44, 179–190. https://doi.org/10.1002/esp.4490.

Naylor, L.A., Stephenson, W.J., 2010. On the role of discontinuities in mediating shore platform erosion. Geomorphology 114, 89–100. https://doi.org/10.1016/j.geomorph.2008.12.024.

NRCS-USDA-Natural Resources Conservation Service-United States Department of Agriculture, Soil Survey Staff, 2003. Soil taxonomy. In: Handbook n° 436. U.S. Department of Agriculture, Washington, DC.

Peel, M.C., Finlayson, B.L., McMahon, T.A., 2007. Updated world map of the Köppen-Geiger climate classification. Hydrol. Earth Syst. Sci. 11, 1633–1644. https://doi.org/10.5194/hess-11-1633-2007.

Piacentini, D., Troiani, F., Torre, D., Menichetti, M., 2021. Land-surface quantitative analysis to investigate the spatial distribution of gravitational landforms along rocky coasts. Remote Sens. 13, 5012. https://doi.org/10.3390/rs13245012.

Pignatelli, R., Giannini, G., Ramírez del Pozo, J., Beroiz, C., Barón, A., 1972. Mapa geológico de España Escala 1:50.000. IGME, Madrid, Spain. N° 15 (14–3) Lastres.

Piñuela, L., García-Ramos, J.C., Ruiz-Omeñaca, J., 2009. Ichnological evidences of gigantic dinosaurs in the late Jurassic of the Iberian Peninsula. J. Vertebr. Paleontol. 29, 164A-A.

Ruiz de Argandoña, V.G., Calleja, L., Suárez del Río, L.M., Rodríguez-Rey, A., Celorio, C., 2005. Durabilidad en ambientes húmedos de la Arenisca de la Marina (Formación Lastres, Jurásico Superior de Asturias). Trab. Geol. 25, 105–115. https://doi.org/10.17811/tdg.25.2005.105-117.

Small, C., Nicholls, R.J., 2003. A global analysis of human settlement in coastal zones. J. Coast. Res. 19, 584–599.

Sunamura, T., 1992. Geomorphology of Rocky Coasts. John Wiley and Sons, Chichester, United Kingdom.

Thiele, S.T., Grose, L., Samsu, A., Micklethwaite, S., Vollgger, S.A., Cruden, A.R., 2017. Rapid, semi-automatic fracture and contact mapping for point clouds, images and geophysical data. Solid Earth 8, 1241–1253. https://doi.org/10.5194/se-8-1241-2017.

Trenhaile, A.S., 1987. The Geomorphology of Rock Coasts. Oxford University Press, Oxford, United Kingdom.

Trenhaile, A.S., 2011. Cliffs and rocky coasts. In: Wolanski, E., McLusky, D.S. (Eds.), Treatise on Estuarine and Coastal Science. Academic Press, Waltham, pp. 171–191.

Trenhaile, A.S., 2014. Climate change and its impact on rock coasts. Geol. Soc. Lond. Mem. 40, 7–17. https://doi.org/10.1144/M40.2.

Trenhaile, A.S., 2018. Shore platform erosion and evolution: implications for cosmogenic nuclide analysis. Mar. Geol. 403, 80–92. https://doi.org/10.1016/j.margeo.2018.05.005.

Troiani, F., Martino, S., Marmoni, G.M., Menichetti, M., Torre, D., Iacobucci, G., Piacentini, D., 2020. Integrated field surveying and land surface quantitative analysis to assess landslide proneness in the Conero promontory rocky coast (Italy). Appl. Sci. 10, 4793. https://doi.org/10.3390/app10144793.

Uzkeda, H., Bulnes, M., Poblet, J., García-Ramos, J.C., Piñuela, L., 2016. Jurassic extension and Cenozoic inversion tectonics in the Asturian Basin, NW Iberian Peninsula: 3D structural model and kinematic evolution. J. Struct. Geol. 90, 157–176. https://doi.org/10.1016/j.jsg.2016.08.003.

Valenzuela, M., García-Ramos, J.C., Suárez de Centi, C., 1986. The Jurassic sedimentation in Asturias (N Spain). Trab. Geol. 16, 121–132. https://doi.org/10.17811/tdg.16.1986.121-133.

Valenzuela, P., Domínguez-Cuesta, M.J., Mora García, M.A., Jiménez-Sánchez, M., 2017. A spatio-temporal landslide inventory for the NW of Spain: BAPA database. Geomorphology 293, 11–23. https://doi.org/10.1016/j.geomorph.2017.05.010.

Valenzuela, P., Domínguez-Cuesta, M.J., Mora García, M.A., Jiménez-Sánchez, M., 2018. Rainfall thresholds for the triggering of landslides considering previous soil moisture conditions (Asturias, NW Spain). Landslides 1, 273–282. https://doi.org/10.1007/s10346-017-0878-8.

Van Maanen, B., Nicholss, R.J., French, J.R., Barkwith, A., Bonaldo, D., Burningham, H., Murray, B., Payo, A., Sutherland, J., Thornhill, G., Townend, I.H., Van der Wegen, M., Walkden, M.J.A., 2016. Simulating mesoscale coastal evolution for decadal coastal management: a new framework integrating multiple, complementary modelling approaches. Geomorphology 256, 68–80. https://doi.org/10.1016/j.geomorph.2015.10.026.

Varnes, D.J., 1978. Slope movement types and processes. In: Schuster, R.L., Krizek, R.J. (Eds.), Landslides, Analysis and Control. Transportation Research Board, National Academy of Sciences, Washington, DC, pp. 11–33. Special Report 176.

Williams, A., Rangel-Buitrago, N., Pranzini, E., Anfuso, G., 2018. The management of coastal erosion. Ocean Coast. Manag. 156, 4–20. https://doi.org/10.1016/j.ocecoaman.2017.03.022.

Young, A.P., Guza, R.T., Flick, R.E., O'Reilly, W.C., Salcedo Gutiérrez, R., 2009. Rain, waves, and short-term evolution of composite seacliffs in southern California. Mar. Geol. 267, 1–7. https://doi.org/10.1016/j.margeo.2009.08.008.